Politecnico di Torino

Master Degree in Environmental and Land Engineering
Climate Change

Geophysical Characterization of Dams: A case study of Aosta Valley (NW Italy)

Supervisor:

Alberto Godio

Co-supervisor:

Chiara Colombero

Valeria Strallo

Candidate:

Paula Lorena Mondino

Graduate Session March 2024

A.a. 2023/2024

Abstract

Dam monitoring is crucial for long-term maintenance and structure safety, particularly for smaller dams, as they are more likely to accidents. For this reason, the PNRR under Nodes project has decided to establish and validate a methodology to characterize and monitor geophysical attributes of earthen embarkments for snow production.

According to Italian legislation, small capacity dams are under the Regional Administration. The monitoring plans implemented by these entities, currently include technical assessments such as standard topographic and geotechnical measures, where these latter are generally carried out with invasive surveys.

Integrating geophysical characterization allows a transition from punctual data provided by these conventional monitoring programs to a more comprehensive view. As a matter of fact, geophysical techniques represent a non-invasive, fast, and effective tool for the characterization and the monitoring of the mechanical parameters of the embankments, which are useful to define the stability of these types of structures.

In this thesis Fourcare dam was taken as test site. This embankment is located in Aosta Valley (NW Italy) at an altitude of 2332 m asl. The dam was built in the nineties with a capacity of 127.120 m3 for snow production by Monterosa S.p.A. The objective of this research was focused on the verification of the mechanical and hydrological properties of the body and its local and global stability, with specific attention to find possible seepage or weakness pathways which could compromise the structure. For the analysis of the hydrological attributes the piezometric levels were considered. Concerning the analysis of mechanical parameters, Electrical Resistivity Tomography (ERT) was implemented with the objective to discover saturated zones. Additionally, Active Seismic surveys were carried out to identify possible structural discontinuities, as well as define mechanical parameters such as Poisson ratio, Young modulus and Shear modulus. For this purpose, P-wave from and S-wave velocities from Seismic Refraction Tomography and Surface Waves were analysed.

From the analysis of seismic velocities, it was possible to observe high values of the mechanical parameters. Whereas, from the ERT results it was possible to highlight the presence of possible saturated zones. However, combining these last observations, with the Shear wave velocities it was concluded that these areas could represent zones of material degradation within the dam structure, potentially leading to weaknesses over time. Therefore, additional analysis and ongoing monitoring programs could provide valuable insights to anticipate future issues.

Acknowledgments

Sommario

List of Figures

1 Introduction

Dams may result from human intervention or natural phenomena like landslides or glacier deposits. Most dams are artificial structures, constructed primarily with earthfill, rockfill, or concrete. These structures fulfil diverse functions, such as storing water for human consumption, supporting agricultural-livestock irrigation, generating hydropower and minimize flooding impact. Furthermore, dams modify river courses by diverting water into canals, tunnels, or artificial reservoirs, enabling recreational pursuits, and meeting various human needs [1].

Large dams have a rich history, symbolizing human progress and our ability to harness nature's resources. This surge in dam construction peaked in the 1970s, with Europe and North America leading the way. By the end of the 20th century, there were over 45,000 large dams worldwide. Then, the focus in these regions has shifted towards managing existing dams [2][3]. While large dams have been recognized for their substantial impacts across various areas including climate, hydrology, biology, and socio-cultural aspects [4], and consciousness of the potentially devastating catastrophes they could release, through historical events like the tragedies at Malpasset (France, 1959), Vajont (Italy, 1963), Banqiao (China), Teton (USA, 1976), Machhu II (India, 1979), among others. International organizations such as the International Commission on Large Dams (ICOLD) and national agencies like the United States Army Corps of Engineering have carefully created

guidelines, standards, and best practices for ensuring dam safety including trough monitoring protocols designed to identify early indicators of deterioration or instability, to reduce potential risks.

However, the majority of dams are not large; estimates suggest that over 800,000 small dams exist worldwide [5]. Despite their prevalence, these structures have not received the same level of study. The significance of small dams should not be underestimated, particularly due to their abundant presence and direct placement within inhabited areas. Many of these smaller structures were constructed decades ago, often under less stringent regulations, due to financial constraints faced by private owners. This holds true for public administrations as well, especially when tasked with managing a large quantity of such dams. Consequently, numerous small dams remain unmonitored, despite their aging infrastructure presenting potential risks to community safety [6][7]. As a result, dam failures are often less dependent on the dam height, with a higher incidence observed among smaller dams. Furthermore, between 1993 and 2018, the annual rate of small dam failures reached 10^{-3}, or one in every 1,000 small dams. This rate is approximately 50 times higher than that observed for large dams during the same period [2] [10].

There is not a standard definition for small-sized dams, it varies widely based on dimensional or parameter criteria. For instance, Swiss legislation considers hydraulic structures higher than 10m, or at least 5m with a reservoir volume greater than 50,000 m3 [8]. In contrast, Brazilian regulations rely on risk category criteria [9], and The United States' Federal Energy Regulatory Commission (FERC) defines small hydropower projects as those with a capacity of 5 megawatts [10]. In the case of The Italian National Technical Code for Dams, small dams are identified by a height under 15m and a reservoir volume under 1,000,000 m^3 and transfer the control and monitoring responsibilities to the regional administration [11].

Moreover, those small hydraulic infrastructure are seeing in increment for snow production after sports winter became more generalized at the beginning of 1970s in the Alps regions, fomenting tourism, and development. Allowing to overcome seasonal difficulty, guarantee the opening and close dates as good ski conditions in strategic sections even for naturally unfavourable expositions resorts. Are usually placed in the section upstream of the snow production system so gravity distribution can be used to supply the network of snow canons. Mainly advantages are permitting water availability in lower water periods, flexibility of filling periods and large volumes to resorts. The first resorts were built at the end of 1980s, with a high increase in 1990s-2000s. By 2006 were 70 in the four departments of the northern French Alps [12]. In Swiss Alps artificial snow cover increase from <10% of the total ski area in 2000 to 36% in 2010 [13]. Meanwhile, in Italy Alps at South Tyrol region, 59% of the ski slopes are covered with artificial snow [14].

According to the IPCC report from 2023, the global surface temperature exhibited an increase of 1.09 °C during the period 2011-2020 compared to the baseline period of 1850-1900. This increase was more pronounced over land, with a rise of 1.59 °C, surpassing the increment observed over the oceans [15]. This temperature rise has significant implications for high-altitude regions like the Alps, where a declining trend in snow cover has been noted and even reducing snow production potential. Projections suggest a considerable rise in the demand for water for snowmaking in the Alps in the near future, estimated to increase by 50% to 110%. This trend is expected to prompt a continued proliferation of high-level reservoirs as a solution for resorts [16][17].

With growing concern over these small hydraulic structures, as previously mentioned, monitoring is primarily conducted through standard topographic and geotechnical measures by regional administrations in Italy. However, these measurements are limited to the scope and are carried out by invasive surveys that could compromise the structure such piezometers and water level indicators. Geophysics, through non-invasive technics allows to understand the hydrodynamics process associated with those structures and even characterize them. Permitting to complement and help to prevent possible dam failures.

Small earth dams are subjected to various case of failures, understanding it as the collapse or movement of any part of the dam or its foundation, resulting in the inability to retain water according to the International Commission on Large Dams (ICOLD). The most prevalent are overtopping, accounting for 31% of cases, followed by internal erosion within the embankment body at 15%, and foundation erosion at 12% [2].

The overtopping process occurs when embankment dams are not designed to handle overflow, and their resistance to failures caused by surface erosion is limited. Once water exceeds the crest, two types of flow develop: one through the dam body and the other as free-surface flow over the dam face. Depending on the construction of the embankment, the duration and magnitude of the overflow event, defined as the head over the crest, different failure modes may occur. A critical area is the downstream toe, where maximal erosion can occur as free-surface flow reaches its maximum velocity. Complete breach of the embankment due to this erosion is referred to as "back cutting" [1].

Subsurface erosion, known as piping, takes place when water displaces soil particles and carries them towards an unprotected exit, forming hidden channels or pipes within a dam or its foundation. Failure happens when the upstream or intake end of the eroded hole nears the bottom of the reservoir. Dam incidents sometimes involve multiple failure modes; for example, the development

of piping through the embankment might result in the saturation of the downstream slope, subsequently leading to overtopping [18][1].

Geophysics, utilizing non-invasive methods like Electrical Tomography and seismic analysis, provides a cost-effective approach to enhance understanding of hydrodynamic processes. This technology can detect abnormal conditions within the dam structure, indicating potential issues such as adverse seepage or changes in flow conditions [19]. Furthermore, it aids in characterizing soil alteration and assessing the compaction techniques used in soil and pavement construction, contributing to a comprehensive evaluation of dam integrity [20].

This thesis is conducted as part of the Nodes project, funded by the PNRR, with the objective of developing and validating a methodology for monitoring the condition of earth embankments used as reservoirs for snowmaking systems. The study focuses to encompass two main perspectives rely on non-invasive geophysical techniques and associated data processing under the Fourcare earth dam in the Aosta Valley, located in the Italian Alps:

1) Assessing Waterproofing Effectiveness: This entails identifying areas impacted by observable or measurable water level reductions within the reservoir and determining potential causative factors.
2) Verification of Dam Mechanical Properties and Slope Stability: This involves examining localized sections of the slopes and overall stability of the reservoir-slope system.

2 Site of Investigation: Fourcare Dam, Aosta Valley

Fourcare is a small earth embarkment built by the Montarosa Ski Company built in 2019 at 2320 m s.l.m over the Bettaforca Italian Alps with a volume of 127.120 m3, to provide artificial snow production to Larici Ski slope, a high-speed chairlift (automating coupling) of 1532 m length built in 1993, which transport 2660 people/hour [32]

As typical Earth dams, the design, construction, and management of retaining barriers (dams and weirs) are based on the Decree of the Ministry of Infrastructure and Transport of June 24, 2014, and the current Technical Standards for Construction of 2018 (abbreviated NTC 2018), A schematic design is illustrated for better comprehension (Figure 1) and 3 typical sections are identified [33] [34]:

- Crest (Coronamiento): represents the top portion, as well as the shorter base of the trapezoid, and its length is proportional to the dimensions of the dam.
- Slopes (Paramenti): are the inclined side surfaces on the upstream and downstream sides.
- Toe (Imposta): is the surface on which the entire dam body rests. It may be necessary to use foundation sealing devices to prevent water from passing through the subsoil, ensuring continuity of the seal, which is achieved on the surface by the central core. For permeable foundation soils, for example, reinforced concrete diaphragms can be added, penetrating through the gravel, and reaching the underlying rock.

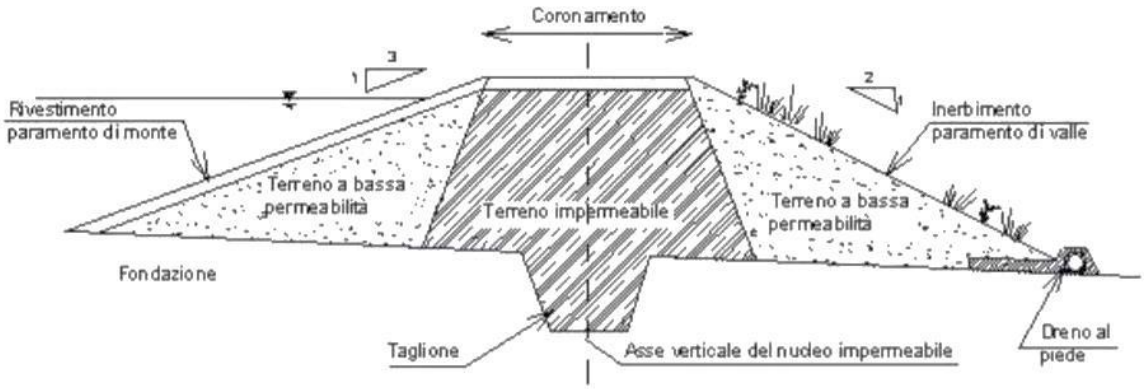

Figure 1 Typical Schematic Earth Dam (Martina Germmato, Foti Sebastiano, Consentini Renato Maria (2021) Tesi di Laurea Magistrale. Comportamento dinamico delle piccole dighe in terra del Piemonte: studio parametrico. Politecnico di Torino)

Based on the previously mentioned, Fourcare embarkment was built following the next proceeds and its Planimetric Plan is shown (Figure 2):

1. **Excavation of the basin bed**: An excavation of approximately 95,000 cubic meters was carried out to create the basin bed, reaching a maximum excavation depth of 11.50 meters below the existing ground level. Excavated material was sieved, crushed, and classified based on size for various purposes.
2. **Placement of lining material**: Fine material was used to cover the basin bed before laying down impermeable membranes. This helped establish a suitable base for waterproofing and ensured the basin's bottom remained watertight.
3. **Construction of drainage system**: After compacting the basin bed, a drainage system was constructed to prevent groundwater accumulation and the lifting of the impermeable bottom. This system collected intercepted water and directed it to a manoeuvring pond for reuse through a pumping system.
4. **Installation of waterproofing**: Two layers of non-woven fabric were placed as a physical separator between strata, upon which the HDPE waterproofing membrane was installed. This ensured the basin's waterproofing and prevented water leaks.
5. **Construction of the shores:** Special attention was given to the morphology design of the shores to naturalize the basin's appearance. They were built with variable slopes and interrupted with terraces to enhance stability and safety. Stones were added to the top of the shores to mitigate visual impact and facilitate environmental integration of the structure.

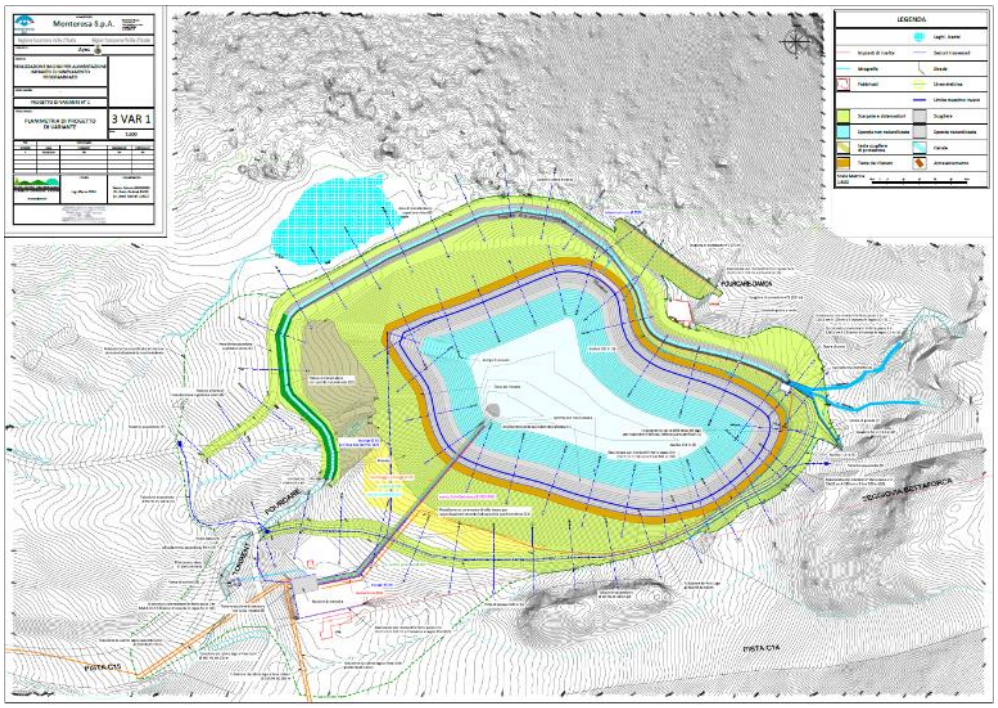

Figure 2 Fourcare Basin Plan in Valle d'Aosta, by Monterosa ski.

As previously outlined, the pursuit of the selected proposed perspectives driven by this thesis and the Nodes project led to the design of the following methodologies, which form the structural framework of this thesis (Figure 3):

- Electrical Resistivity Tomography (ERT) with Dipolo-Dipolo and Wanner configurations to characterize materials and potentially detect discontinuities affected by filtration phenomena (referenced as ERT in Figure 3)
- Seismic Refraction Tomography for analysing compression wave behaviour using vertical geophones to assess material mechanical properties and identify potential structural discontinuities within the dam body (referenced as S in Figure 3)
- Surface wave velocity measurements to estimate shear wave velocity distribution, in conjunction with P-wave measurements, for evaluating the mechanical properties of the dam body.

Figure 3 ERT and Seismic Surveys performed at the basing of the Fourcare Embarkment to assess Thesis and Nodes Project Objectives

3 Electrical Resistivity Tomography

3.1 Introduction

ERT is one of the most well-established and widely applicable geophysics method for measuring material resistivity to detect soil properties, geological structure, seepage, cracking, and presence of metallic objects.

3.2 Working Principle

It consists in creating an electrical potential difference in the subsurface due to an injection of electric current though two electrodes (A, B) and measuring the voltage difference across two potential electrodes (M, N) (Figure 4). For each transmitted current a voltage induced is recorded and, according to Ohms law, it is obtained an apparent resistivity which conform a pseudo section, a preliminary display of ERT data. Therefore, an inversion procedure of the data is performed to estimate the ground resistivity distribution.

Usually, a battery run power apply a direct current (DC) into a first pair of electrodes and a symmetrical distance a second pair measures the resulting apparent resistivity. Measurements are taken for different 4-electrode combinations, shifting each time by one electrode separation laterally until the appropriate number of levels have been scanned. Meanwhile the space between them increase also does depth but resolution decrease. Electrodes are connected by a multi-core cable to a switching box and a resistance meter or by a single cable, typically of 72 or more. The whole data acquisition is controlled by a software from a laptop computer.

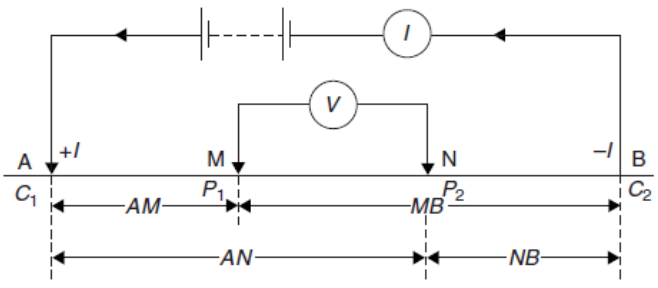

Figure 4 ERT Schematic principle ()

Figure 5 . Single cable of 72 electrodes of electrical resistivity tomography survey performed in July 2023 at Fourcare dam, Valle d'Aosta.

Figure 6 Laptop and resistance meter from electrical resistivity tomography survey performed in July 2023 at Fourcare dam, Valle d'Aosta.

3.3 Application to Fourcare Dam

They were performed 6 electrical lines installed at various levels along the downstream embarkment and transversely, as follows (Fig. 3):

- Line No.1: Consists of 72 electrodes spaced at 3-meter intervals, positioned on the crest, utilizing Wanner and Dipolo-Dipolo electrode configuration.
- Line No.2: Comprises 72 electrodes spaced at 3-meter intervals, also positioned on the crest, employing Wanner and Dipolo-Dipolo electrode configuration.
- Line No.3: Includes 42 electrodes spaced 2 meters apart, extending from the slope towards the crest, utilizing Wanner and Dipolo-Dipolo electrode configuration.
- Line No.4: Comprises 24 electrodes spaced 2 meters apart, extending from the slope towards the crest, utilizing Wanner and Dipolo-Dipolo electrode configuration.
- Line No.5: Consists of 48 electrodes spaced 2 meters apart, installed along the slope, utilizing Wanner and Dipolo-Dipolo electrode configuration.
- Line No.6: Includes 48 electrodes spaced 2 meters apart, also installed along the slope, utilizing Wanner and Dipolo-Dipolo electrode configuration.

3.4 Data processing

The provided data was already converted into matrix format to be analysed. Therefore, the data processing consisted on the filtering and checking quality data with Prosyslll to perform the Electrical Tomography Inversion in ResIPY (Figure 7).

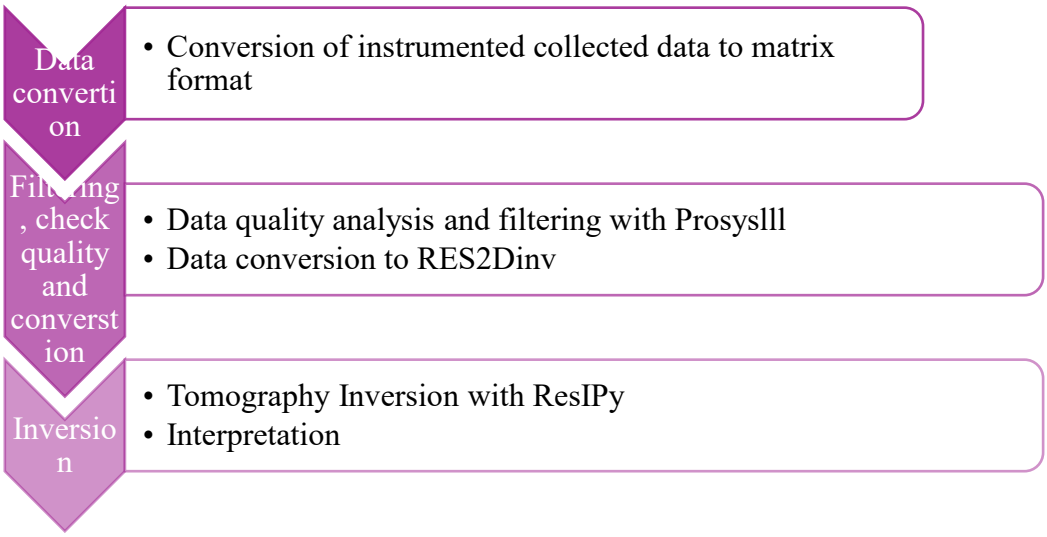

Figure 7 Scheme Data processing for Electrical Resistivity Tomography.

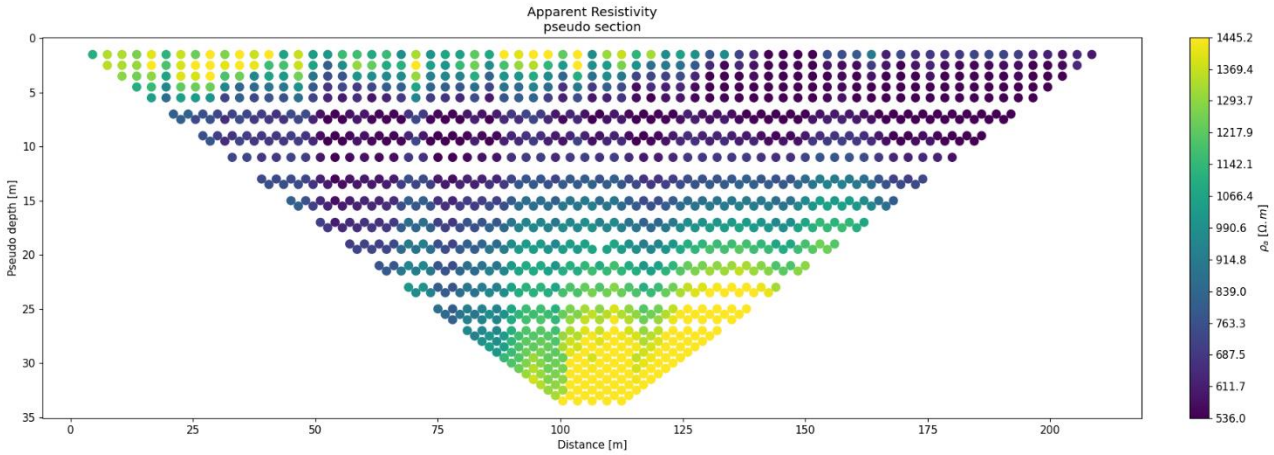

Figure 8 Pseudosection of Wanner configuration from ERT 1 with 3m spacing.

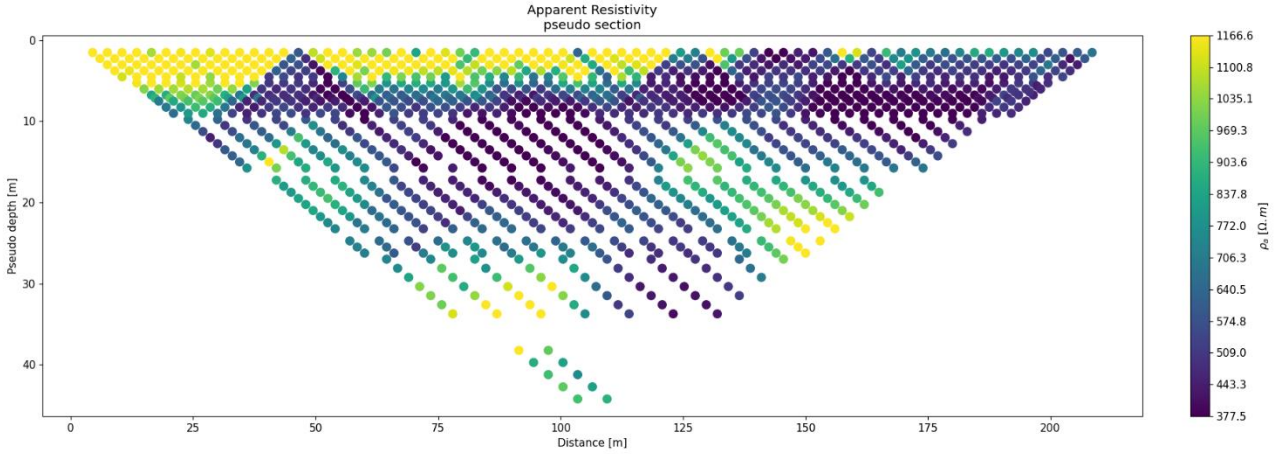

Figure 9 Pseudosection of Dipolo-Dipolo configuration from ERT 1 with 3 spacing.

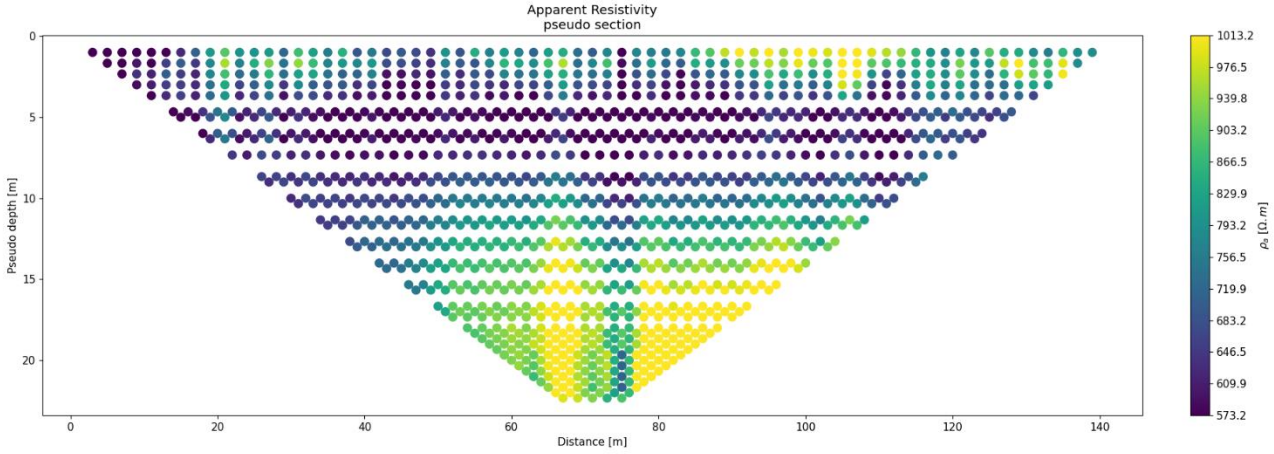

Figure 10 Pseudosection of Wanner configuration from ERT 2 with 2m spacing.

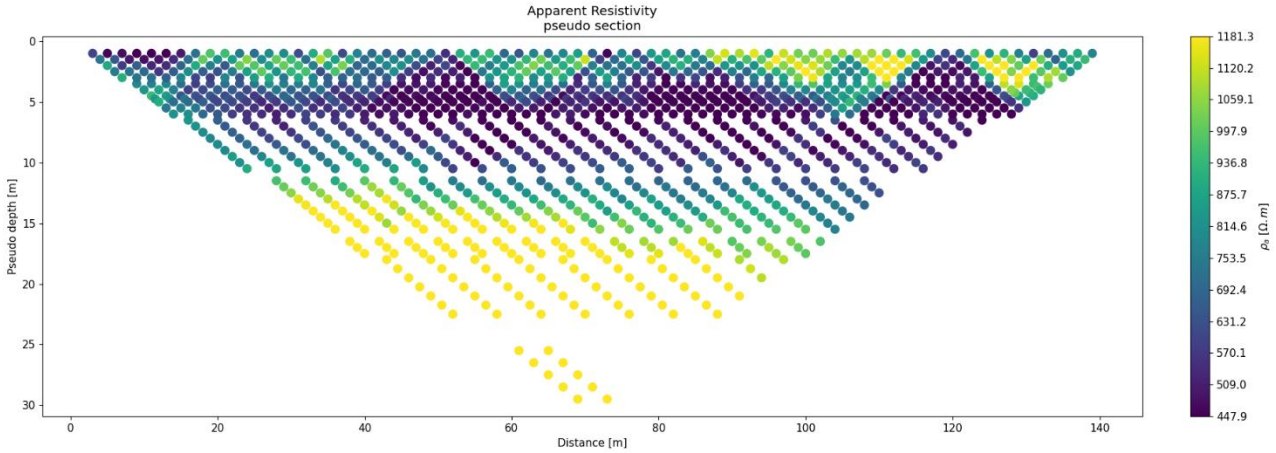

Figure 11 Pseudosection of Dipolo-Dipolo configuration from ERT 2 with 2 spacing.

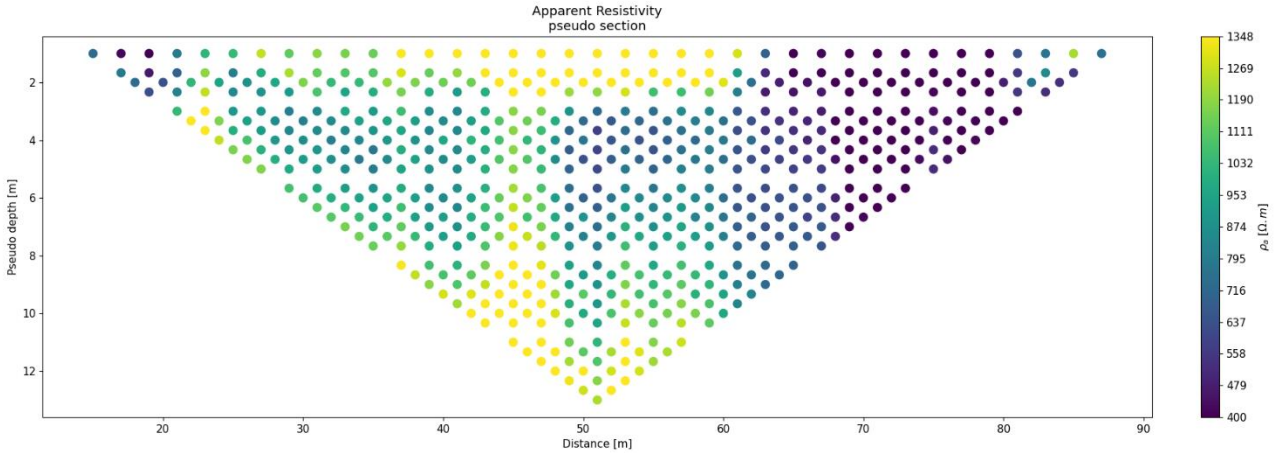

Figure 12 Pseudosection of Wanner configuration from ERT 3 with 2m spacing.

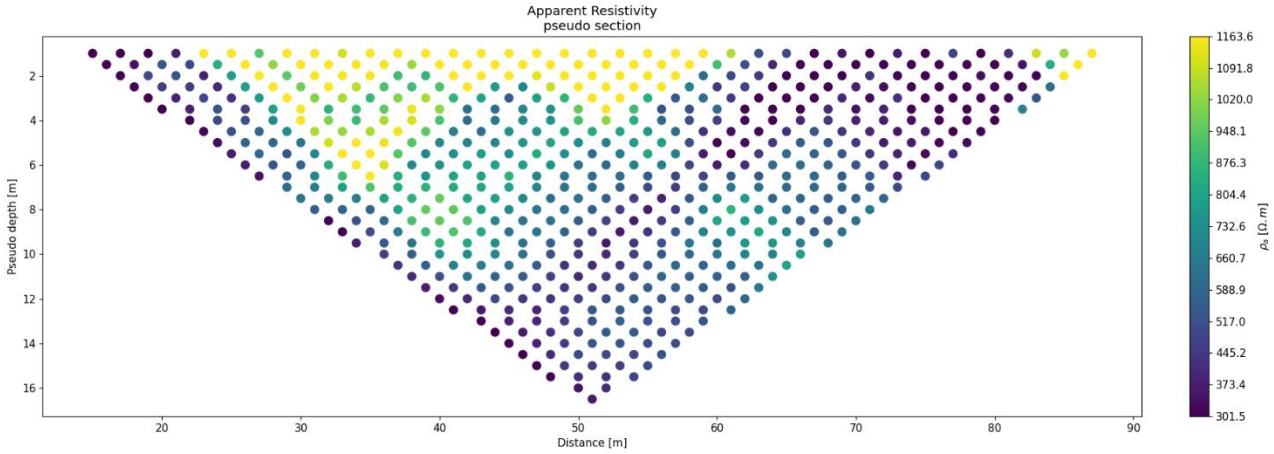

Figure 13 Pseudosection of Dipolo-Dipolo configuration from ERT 3 with 2m spacing.

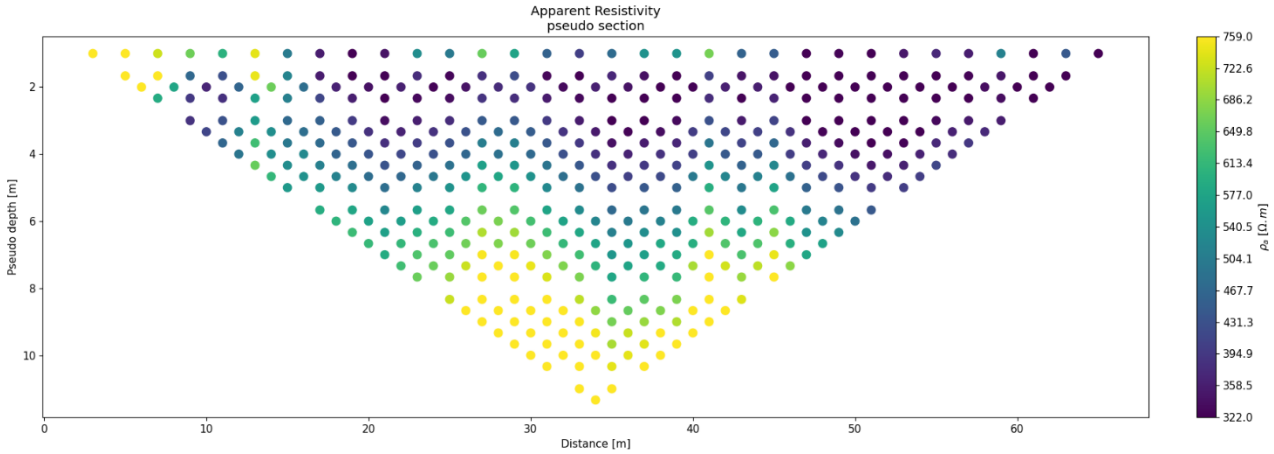

Figure 14 Pseudosection of Wanner configuration from ERT 5 with 2m spacing.

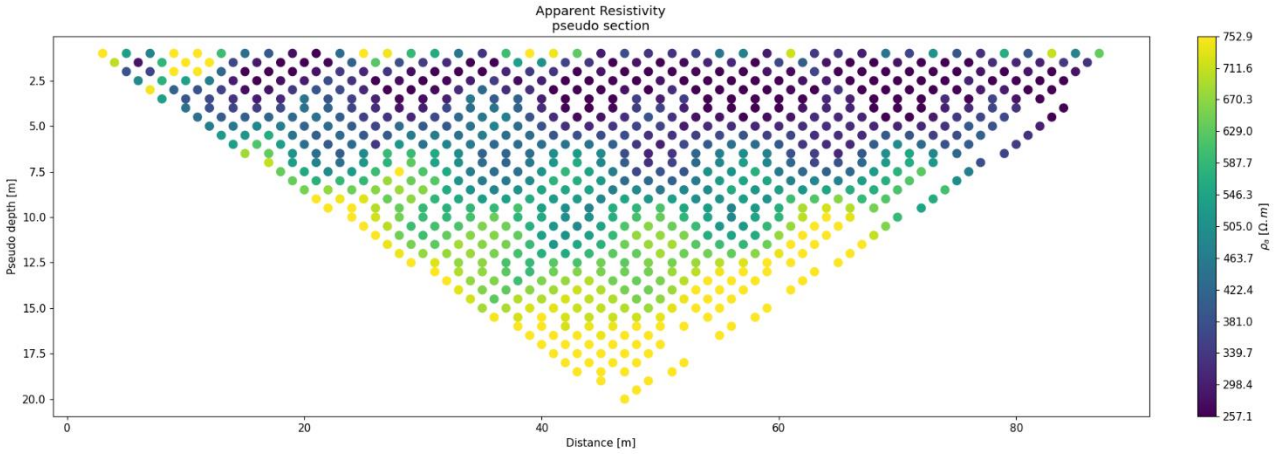

Figure 15 Pseudosection of Dipolo-Dipolo configuration from ERT 5 with 2m spacing.

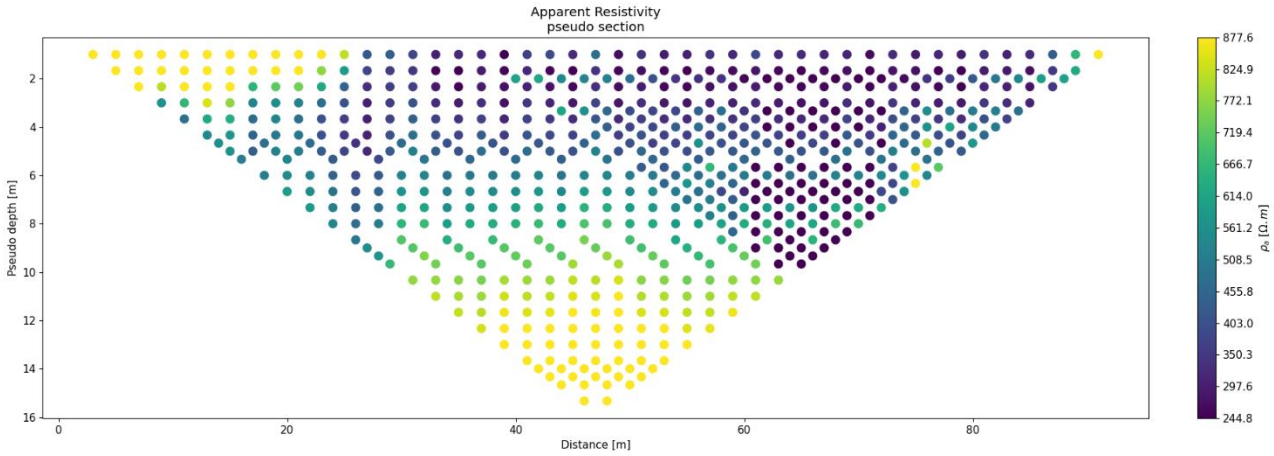

Figure 16Pseudosection of Wanner configuration from ERT 6 with 2m spacing.

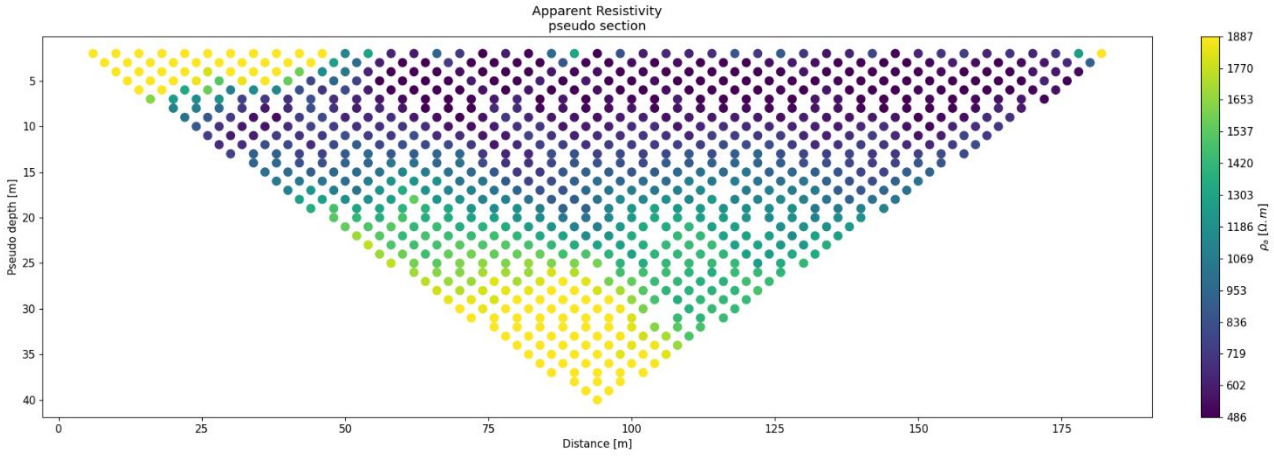

Figure 17 Pseudosection of Dipolo-Dipolo configuration from ERT 6 with 2m spacing.

3.5 Results

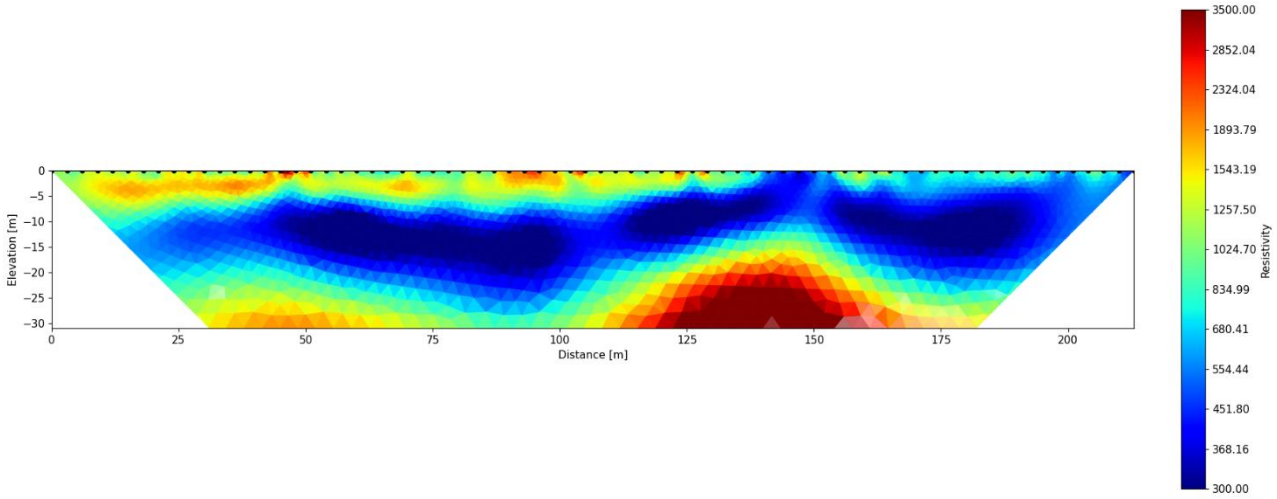

Figure 18 Electrical Resistivity Tomography 1 with Wanner Configuration of 3m spacing 72 electrodes.

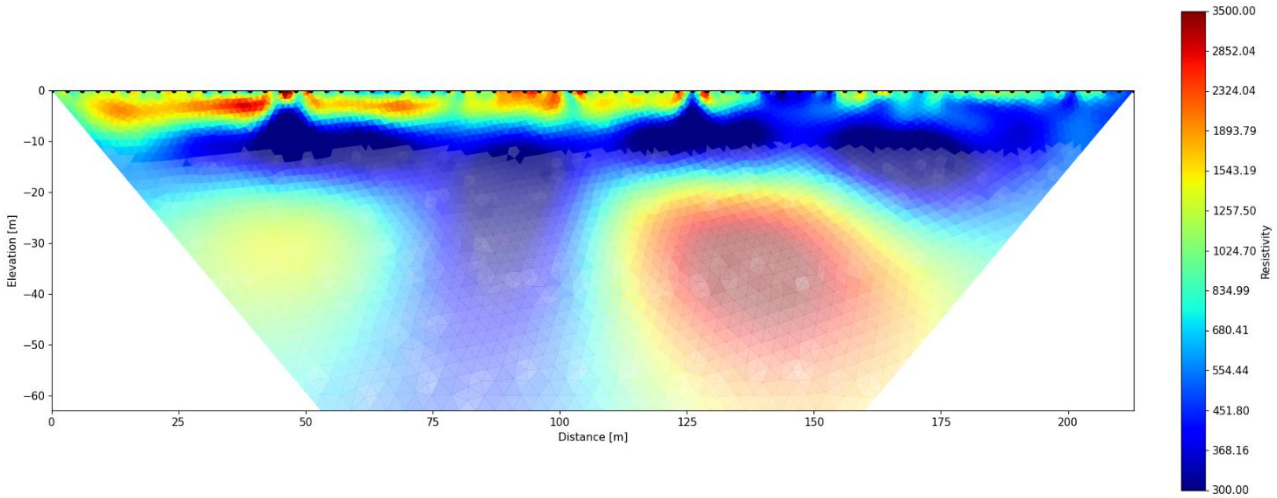

Figure 19 Electrical Resistivity Tomography 1 with Dipolo-Dipolo Configuration of 3m spacing 72 electrodes.

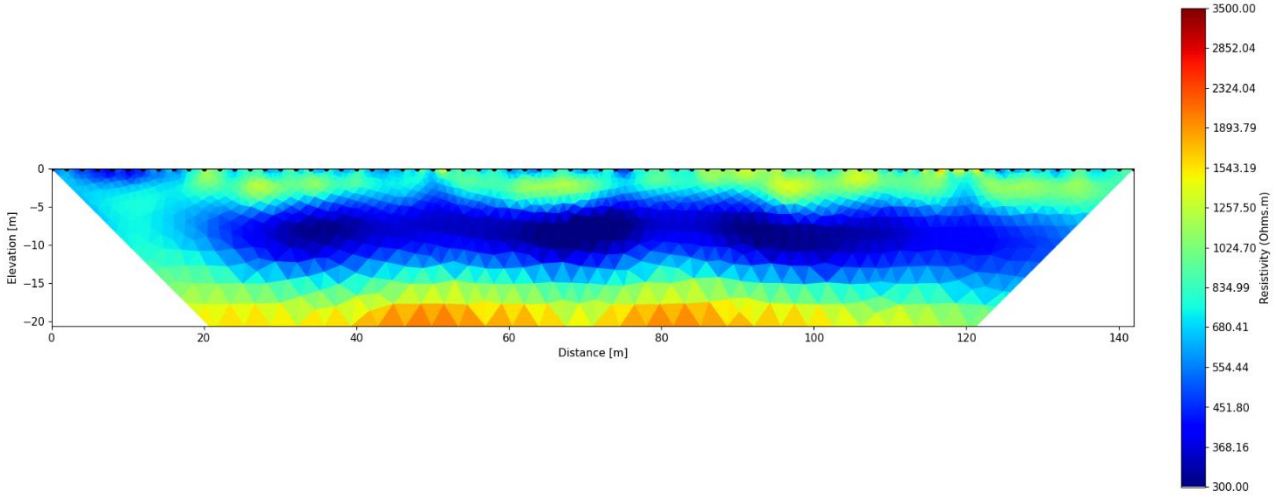

Figure 20 Electrical Resistivity Tomography 2 with Wanner Configuration of 2m spacing 72 electrodes.

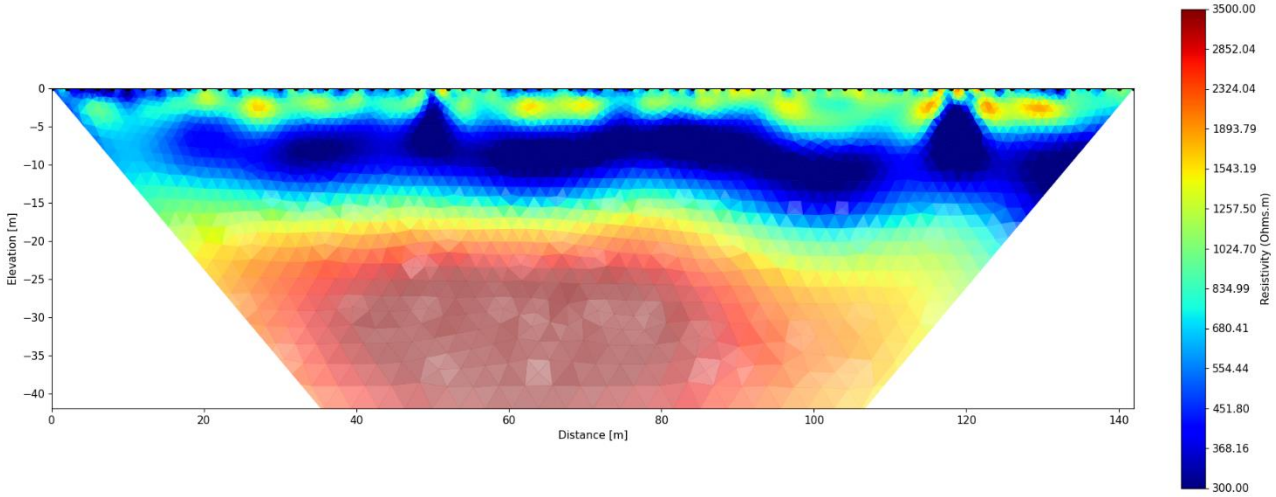

Figure 21 Electrical Resistivity Tomography 2 with Dipolo-Dipolo Configuration of 2m spacing 72 electrodes.

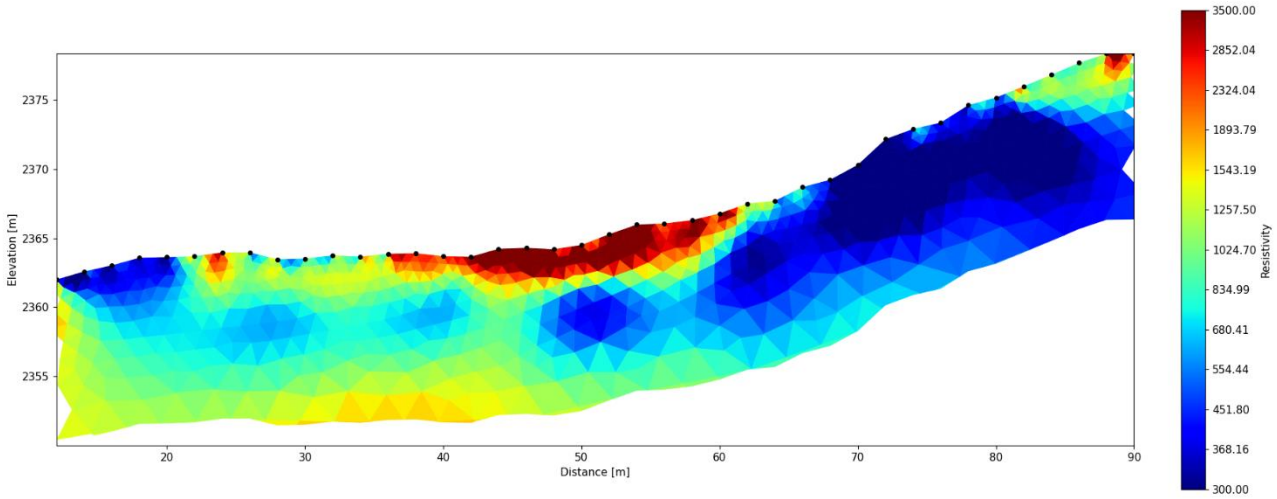

Figure 22 Figure 19 Electrical Resistivity Tomography 3 with Wanner Configuration of 2m spacing 45 electrodes.

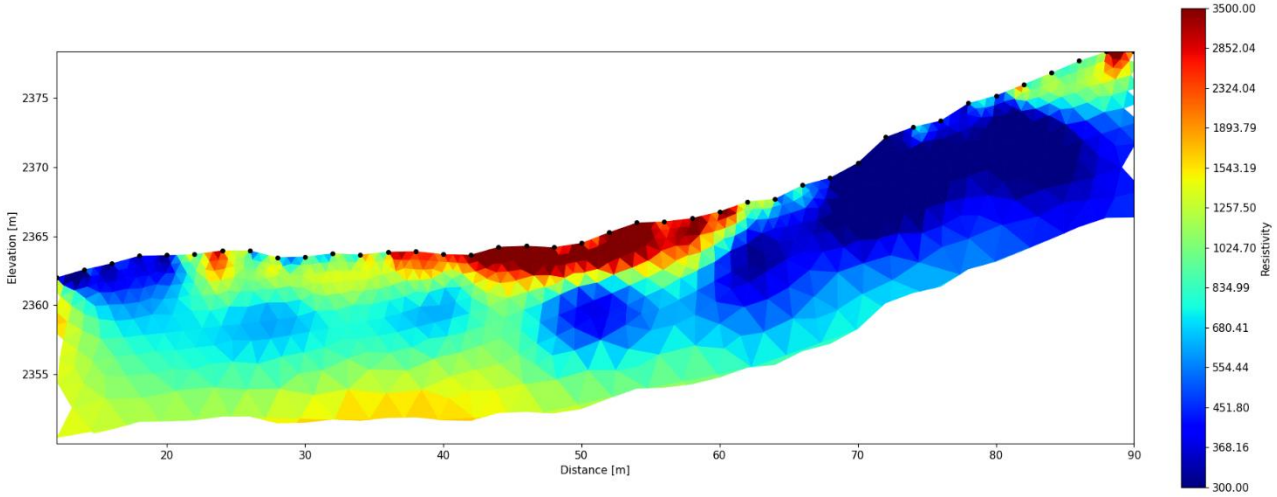

Figure 23 Electrical Resistivity Tomography 3 with Dipolo-Dipolo Configuration of 2m spacing 45 electrodes.

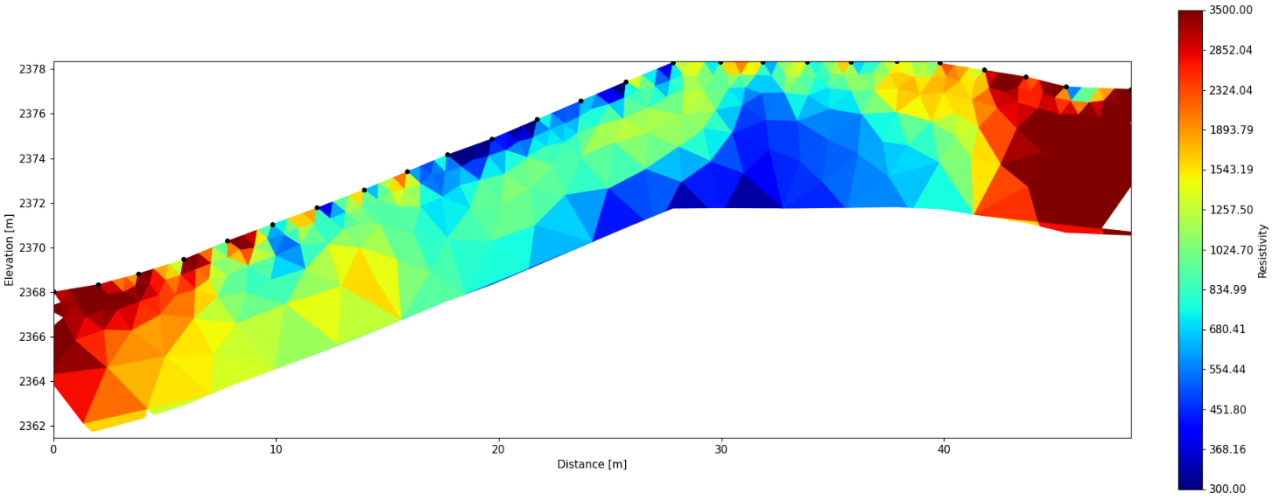

Figure 24 Electrical Resistivity Tomography 4 with Wanner Configuration of 2m spacing 24 electrodes.

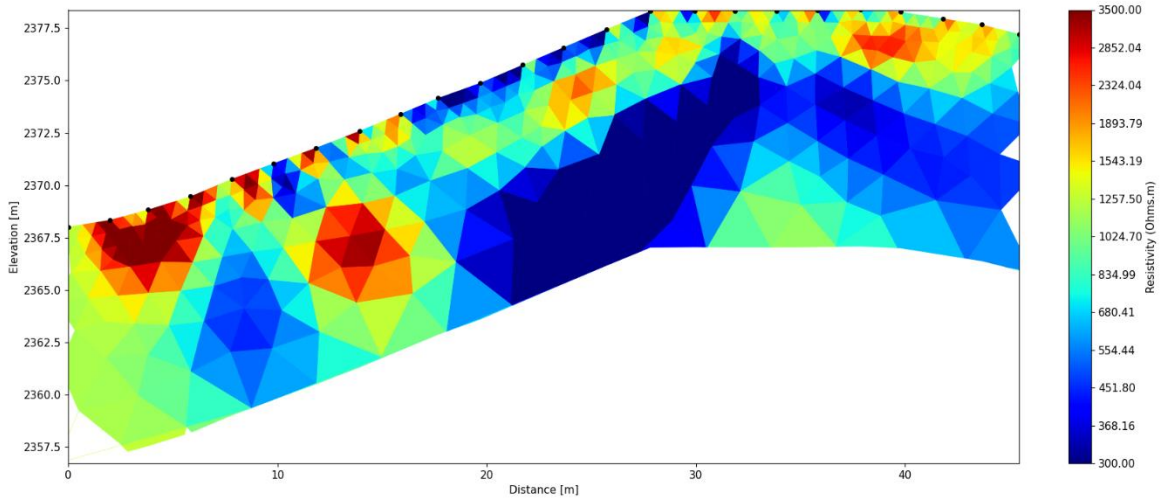

Figure 25 Electrical Resistivity Tomography 4 with Dipolo-Dipolo Configuration of 2m spacing 24 electrodes.

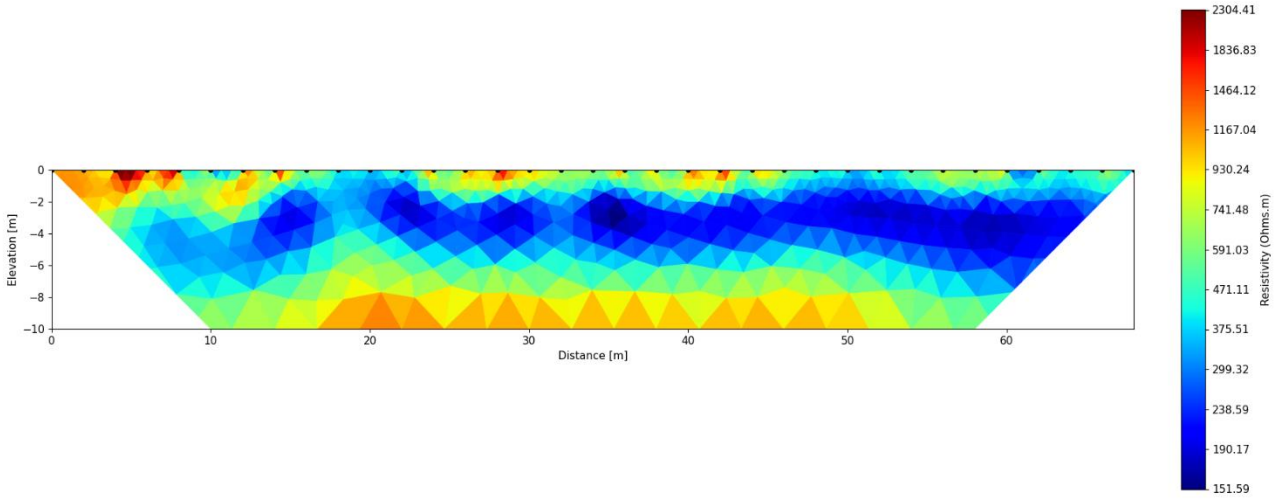

Figure 26 Electrical Resistivity Tomography 5 with Wanner Configuration of 2m spacing 35 electrodes.

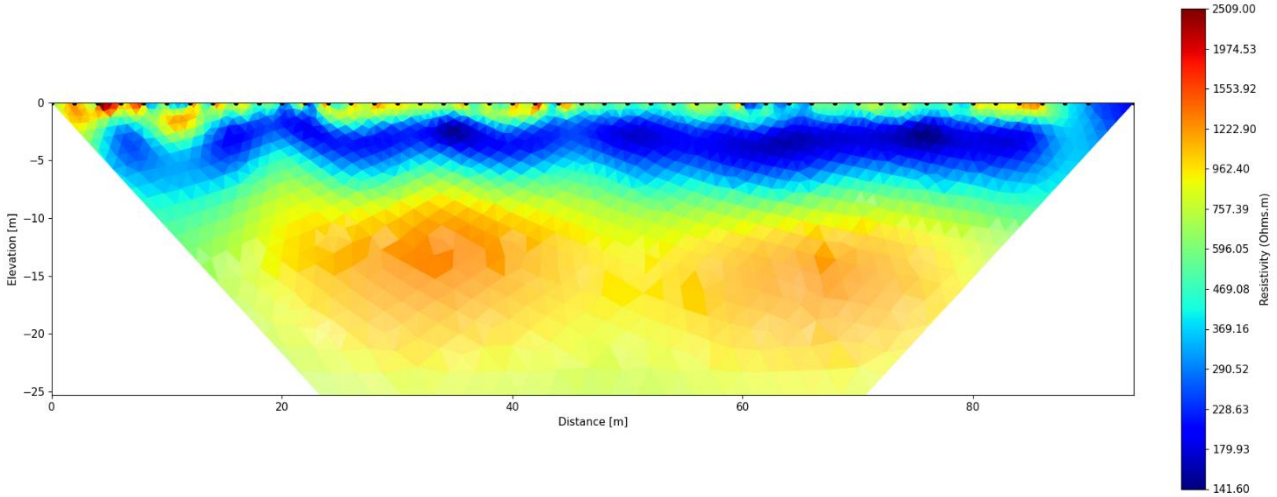

Figure 27 Electrical Resistivity Tomography 5 with Dipolo-Dipolo Configuration of 2m spacing 48 electrodes.

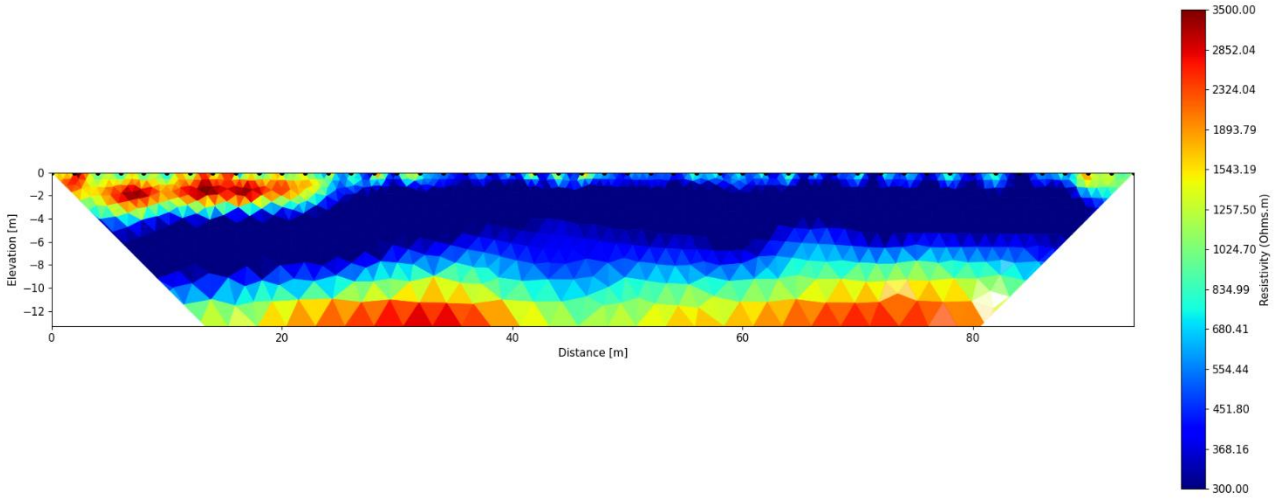

Figure 28 Electrical Resistivity Tomography 6 with Wanner Configuration of 2m spacing 48 electrodes.

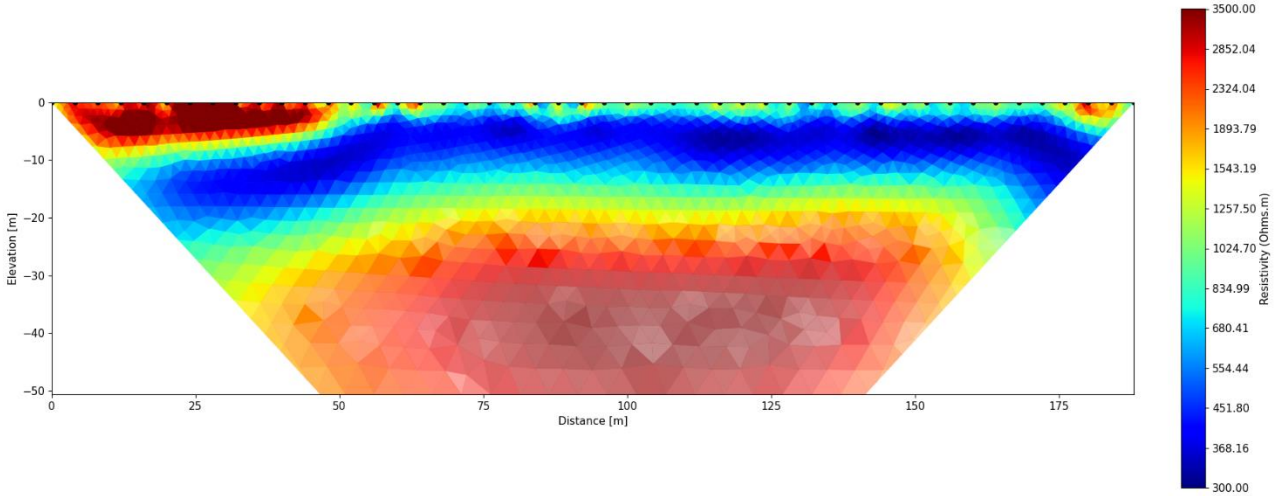

Figure 29 Electrical Resistivity Tomography 6 with Dipolo-Dipolo Configuration of 2m spacing 48 electrodes.

Active Seismic

A seismic source emits energy in the form of elastic strain, and the velocity of seismic waves is contingent upon the elastic moduli and densities of the media they traverse. These waves are categorized as 'body waves' when traversing through the bulk of the medium and as 'surface waves' when confined to interfaces between media with contrasting elastic properties. Among these, the most significant in exploration seismology are P-waves, where material particles oscillate about fixed points in the direction of wave propagation due to compressional and dilational strain. The second type, S-waves, involve particle motion perpendicular to the wave propagation direction, occurring through pure shear strain.

In contrast, surface waves, such as Rayleigh waves, do not penetrate subsurface media. They travel along the free surface, with their amplitude decreasing exponentially with depth. Particle motion occurs solely within the solid medium, in a retrograde elliptical pattern in a vertical plane relative to the surface. Love waves, on the other hand, exhibit particle motion perpendicular to the direction of wave propagation, parallel to the surface. They only occur when a medium with high S-wave velocities underlies a medium with low S-wave velocities [21].

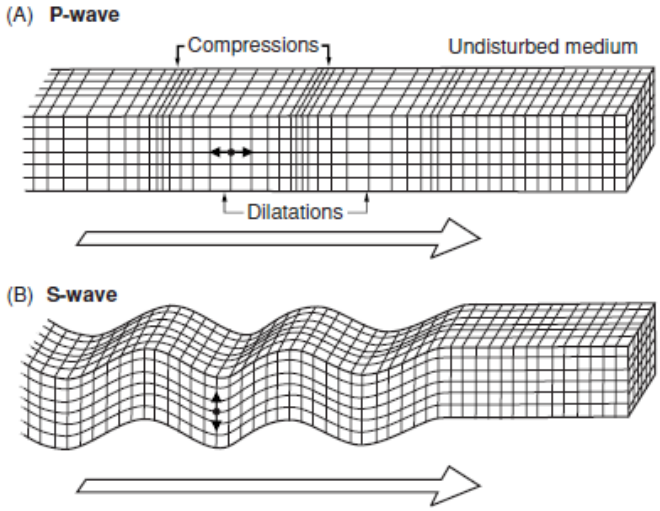

Figure 30 Elastic deformation and ground particle motion in body waves (A) P-waves (B) S-waves (John M. Raynolds, An introduction to applied and environmental geophysics 2nd edition)

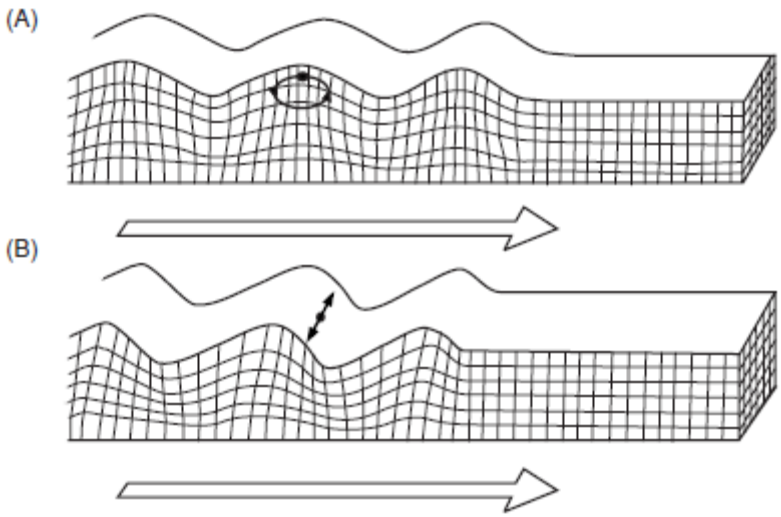

Figure 31 Elastic deformation and ground particle motion in surface waves (A) Rayleigh wave (B) Love wave (John M. Raynolds, An introduction to applied and environmental geophysics 2nd edition)

When a seismic signal encounters the boundary between two elastic media, a portion of the wave energy is reflected while the rest is refracted, leading to a P-to-S conversion phenomenon. A surface where all particles are at the same phase of motion is referred to as a wavefront. Huygen's Principle postulates that each point on this wavefront can be consider as a secondary source, thus seismic waves are examined in terms of rays and raypaths [22]

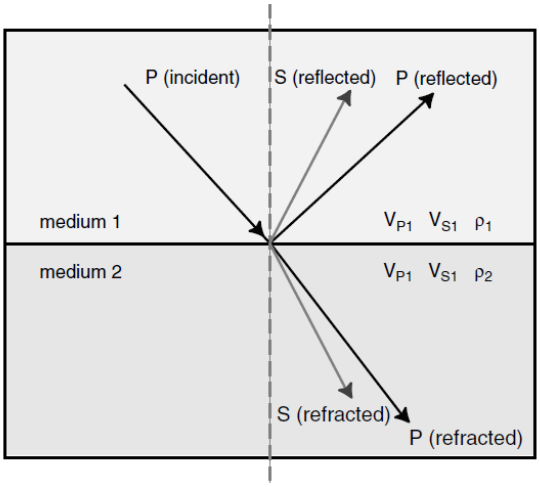

Figure 32 P-to-S conversion at an interface (Mark E. Everett (2013). Near Surface Applied Geophysics. Cambridge University Press)

The angle of incidence and the angle of reflected waves are equal, following the law of reflection. Meanwhile, the direction of the transmitted wave changes according to Snell's law, which describes refraction. The amplitudes of these waves are described by the Zoeppritz equation, revealing that most of the incident energy is divided into reflected and refracted P-waves, with only a small portion allocated to reflected and refracted S-waves.

Equation 1

$$\frac{\sin i}{Vp1} = \frac{\sin r}{Vp2} = p$$

In the equation, "i" and "r" stand for the incident and refraction angles, while 'V1' and 'V2' represent the propagation speeds in layers 1 and 2, respectively. Additionally, "p" is used to denote the raypath parameter.

4.1 Refraction

4.1.1 Introduction

When the angle of incidence reaches 90°, it is termed the critical angle. At this point, the refracted wave travels along the upper boundary of the lower medium, where the propagation speed and thickness are higher than the overlaying medium, and each thickness layer is greater than the wavelength of the incident energy. Head waves are generated at the interface due to an oscillating stress caused by the passage of the refracted wave, eventually reaching the surface through upward-moving waves.

Equation 2

$$i_c = sin^{-1}\frac{V1}{V2}$$

Where 'ic' represents the "critical angle," and 'V1' and 'V2' denote the propagation speeds in layers 1 and 2, respectively. In refraction surveys, P-waves are commonly utilized and generated by a seismic source. These waves travel through three primary paths: along the top ground surface as "direct waves," reflecting from the top of the reflector, and experiencing critical refraction along the top of the refractor. It could occur,

4.1.2 Working Principle

In recent years, seismic refraction methods have seen increased utilization in near-surface geophysical investigations. To address challenges such as mapping discrete bodies, cavities, and pollution plumes, cutting-edge techniques are being employed. Seismic Refraction Tomography (SRT), which involves the use of multiple shot points, allows for the fitting of more flexible models, resulting in high-resolution subsurface profiles that cover larger areas compared to conventional methods.

SRT data acquisition involves survey lines comprised of channels of geophones, which serve as electrochemical transducers, detecting wave arrivals by converting ground motion into electrical signals. These geophones are connected to a seismograph via geophone cables for recording and housing the collected information. Subsequently, all field data is transferred to a laptop for analysis. The output of each geophone is displayed as a single trace and picking the first arrival times a time-distance graph is plotted to reconstruct ray paths into the ground by numerical models. SRT survey lines are designed based on the transverse length, geometry of the target point, and depth of investigation. Greater depths can be achieved by increasing the energy source at shot points [23].

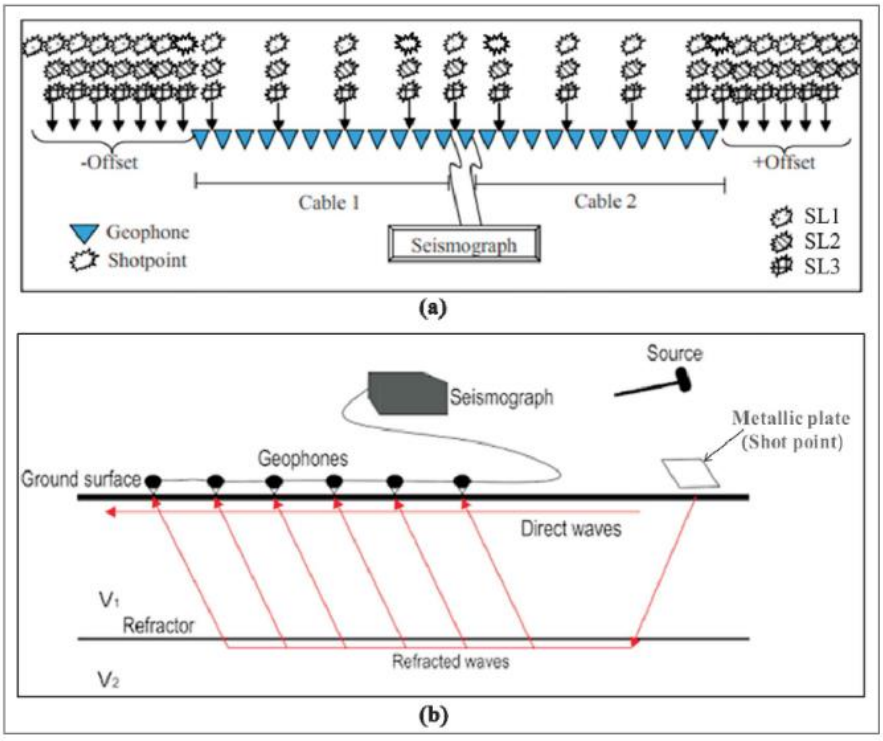

Figure 33 (a) Scheme of typical seismic refraction tomography data acquisition, showing channel of geophones, cables connected to seismograph and shot point location for every survey line (b) instrument and progression of seismic P-waves generated at the surface and reflected boundary surfaces during data acquisition (Akingboye Adedibu Sunny, Ogunyele Abimbola Chris, 2019)

To perform geophysical inversion, it is necessary to find the subsurface model whose response fits the observed data best (Eq. 3). Generally geophysical applications deal with mixed-determined problems, where some model parameters are overdetermined and other underdetermined, implying non-lineal model functions, thus is obtained by applying Taylor expansion about the model function about the model parameters m^{est} in the classical inverse lineal solution least square method (Eq. 4), and considering only primer order terms, the solution over non-linearised function is obtained (Eq. 5).

Equation 3

$$observed\ data\ (d) \rightarrow model\ f(d,m) \rightarrow estimatesof\ model\ aprameters\ (m^{est})$$

Equation 4

$$E = \sum_{i=1}^{N} e_i^2 = \sum_{i=1}^{N} (d_i - d_i^{pred})^2$$

Equation 5

$$\Delta d = G\Delta m$$

Where $\Delta d = d^{obs} - g(m^{est})$ and $G = \frac{\partial g}{\partial m^{est}}$ is the Jacobian matrix relating changes in the model data to change in the model parameters. Finally, model parameters misfit (Eq. 6) can be solved by iteration with the new estimated model parameters m^{est} determined from the data misfit Δd.

Equation 6

$$\Delta m = m - m^{est}$$

In Seismic Refraction Tomography (SRT), the process entails inverting measured seismic travel time data to derive the seismic velocity within each model cell. However, this is restricted to blocks intersected by rays (Figure 34). To address ambiguous solutions during inversion, where some data may not be individually resolved, constraints such as damping and/or model smoothness are employed (Eq. 7), where h=Dm (Eq. 8), I represent the identity matrix, S denoting a Laplacian smoothing matrix, and λ controlling the total regularization applied. The parameter β, varying from 0 to 1, determines the relative importance of damping and smoothing.

Assessing the inversion's quality entails analysing both model resolution and accuracy, which depend on the number of model parameters corresponding to the model blocks. Regions with abundant ray coverage exhibit higher resolution, whereas those with limited ray coverage demonstrate lower resolution. Consequently, this yields a distinct yet locally incomplete depiction of the subsurface [24].

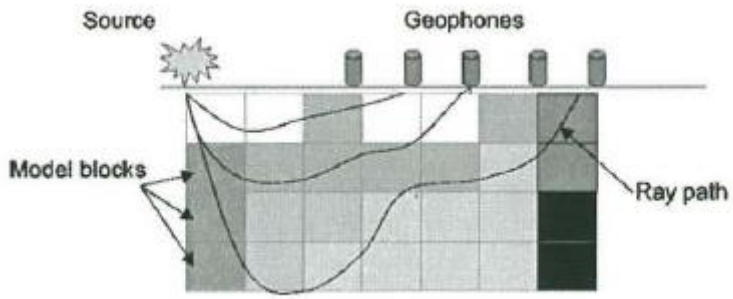

Figure 34 Scheme of Seismic Tomography Principle, where P-wave velocities of each block model is determined by the inversion process (Christian Hauck, Zurich 2001. Geophysical methods for detecting permafrost in high mountains. Technical Note 171. Mitteilugen).

Equation 7

$$\frac{d}{h} = \frac{g}{d} * m$$

Equation 8

$$\left(\frac{\lambda\beta m_0}{0}\right) = \left(\frac{\lambda\beta \mathrm{I}}{\lambda(1-\beta)\mathrm{S}}\right) m$$

4.1.3 Application at Fourcare Dam

Three Seismic surveys were conducted along the perimeter of the ridge overlooking the valley to identify potential areas of filtration. A 10 kg sledgehammer was utilized as a source, generating waves detected by a geophone at a sampling rate of 250 Hz. The collected data was meticulously recorded and managed using Seismodule Controller Software (SCS) was formatted into Seg-2 binary data for subsequent analysis. In dentail, the surveys were executed as follows:

- Seismic Survey 1: Utilized 72 geophones positioned 2 meters apart along a stretch of 142 meters. Energy was applied by striking a steel plate at every 4 geophone intervals, with each position repeated 5 times.
- Seismic 2: Employed the same setup as Seismic Survey 1, with 72 geophones spaced 2 meters apart with an intentional overlap at the 25th geophone position from Seismic Survey 1, covering a total length of 192m. Energy application followed the same methodology, striking the steel plate at every 4 geophone intervals and repeating 3 times per position.
- Seismic Survey 3: Similar to Seismic Survey 1, this survey utilized 72 geophones spaced 2 meters apart along a 142-meter length. Energy application followed the same pattern, striking the steel plate at every 4 geophones and repeating 5 times per position.

4.1.4 Data processing

As previously detailed, Seismic Refraction Tomography (SRT) relies on seismic refraction, especially the analysis of P-waves, the earliest arrivals in shot gatherings. Thus, through utilization of numerical models, data undergoes processing to construct a velocity model of the subsurface (Figure 35).

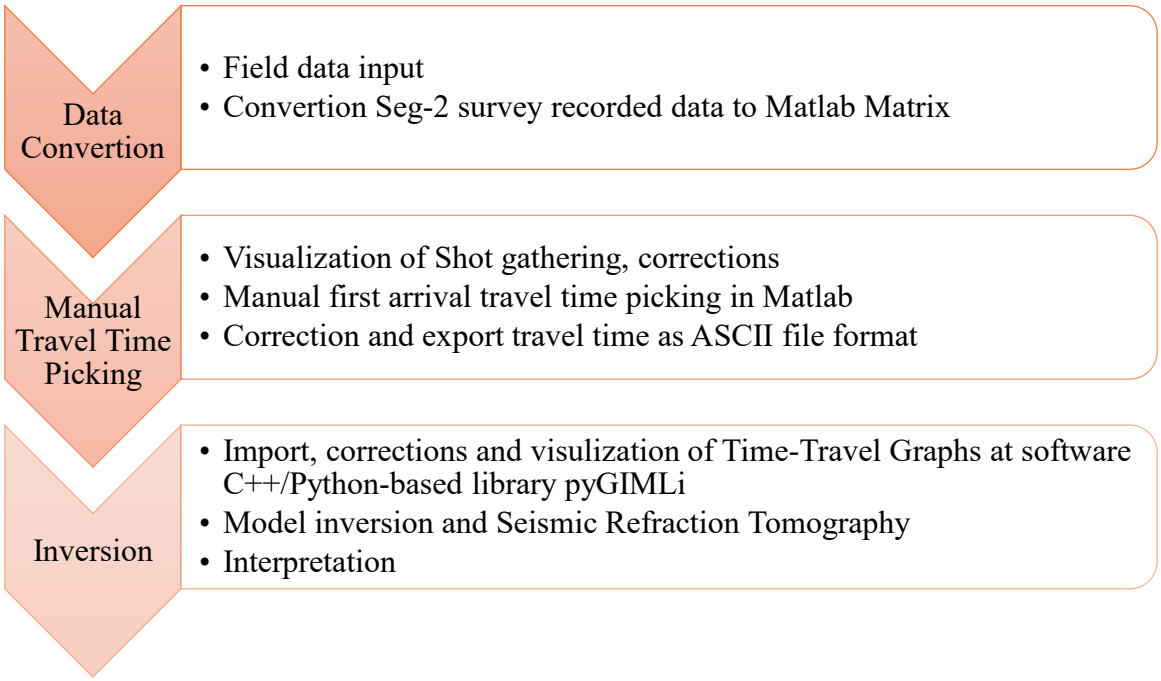

Figure 35 Scheme Data Processing for Seismic Refraction Tomography

In the initial phase, all shot gathers underwent conversion from their Seg-2 binary format to a structured MATLAB matrix. This matrix comprised the source location, geophone vector, number of samples, and traces, organized into rows and columns, respectively. Following this transformation, data integrity was verified to ensure that geophone offset, source, and shot positions were aligned. This facilitated the utilization of the MATLAB wiggle function, which renders two-dimensional scalar fields on a horizontal plane, enabling the observation of a time-distance plot—a representation of seismic traces recorded by each geophone. The shot position is discerned by identifying the geophone where the initial wave arrival registers the shortest time (Figure 36).

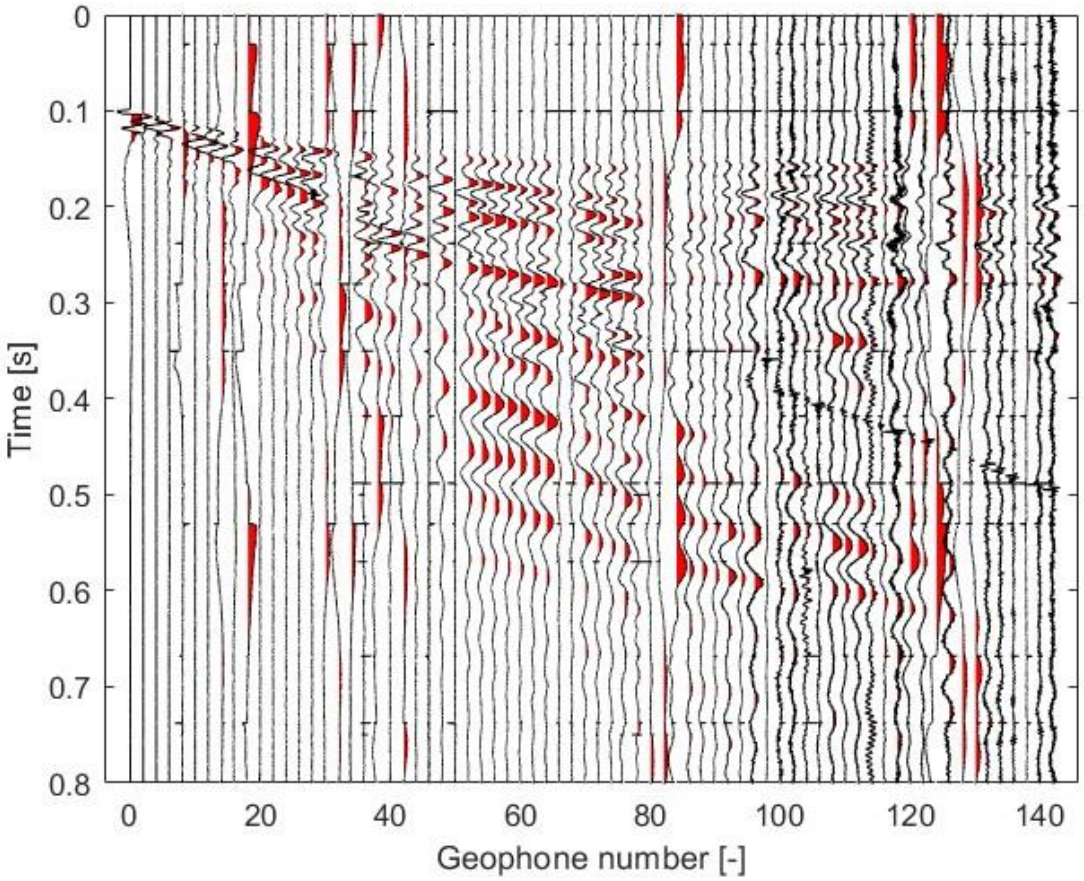

Figure 36 Time-distance plot by a seismic tracing recorded in Seismic Survey 1. As it can see, shot position corresponds to geophone 1, which is found at 0m position.

Therefore, the manual determination of the initial arrival time, indicative of the P-wave, was executed on individual traces with reference to the shot gather. This process was facilitated through a MATLAB script featuring a wiggle function, enabling manual identification of the first arrival times [25]. The process comprised the following steps:

1. **Identifying Arrivals on the Shot Gather**: Direct arrivals, particularly P-waves originating directly from the shot, were pinpointed on the shot gather.
2. **Picking Individual Traces**: with the arrivals identified on the shot gather, it was proceeded to pick those arrivals on the individual traces within the shot gather dataset. Involved visually inspecting each trace within the shot gather dataset and marking the time of identified arrivals. This process utilized a script that visualized traces using the Wiggle function, with a zoom applied to the area of interest for enhanced accuracy. First arrival times were manually marked along the geophone position with a left mouse click. Due to noise recorded, there were initial arrivals difficult to identify, and the picking process was selectively skipped on some geophones. The process concluded with a right-click of the

mouse. Each picked time was compared to the minimum value in the corresponding individual trace, referencing the data respect to its shot position.

3. **Using the Shot Gather as a Guide**: The picks made on individual traces are guided by the arrivals observed on the shot gather, to ensure consistency and accuracy in identifying the same arrivals on each trace. The waveform characteristics and relative arrival times on the shot gather serve as reference points for picking arrivals on individual traces.
4. **Quality control**: post-arrival picking to ensure consistency across all traces was conducted. This involved plotting all time-travels collectively to confirm that at the shot position of each individual trace, the arrival time corresponded to 0. Any anomalies were identified and removed, considering the tendency for arrival times to increase with depth. Moreover, it was verified that the first and last shots exhibited similar travel times, serving as a benchmark to remove over picked arrival times. This process ensured data uniformity and enhanced consistency, laying a robust foundation for subsequent inversion and analysis. An example of the proceed can be seen at (Figure 37).

.

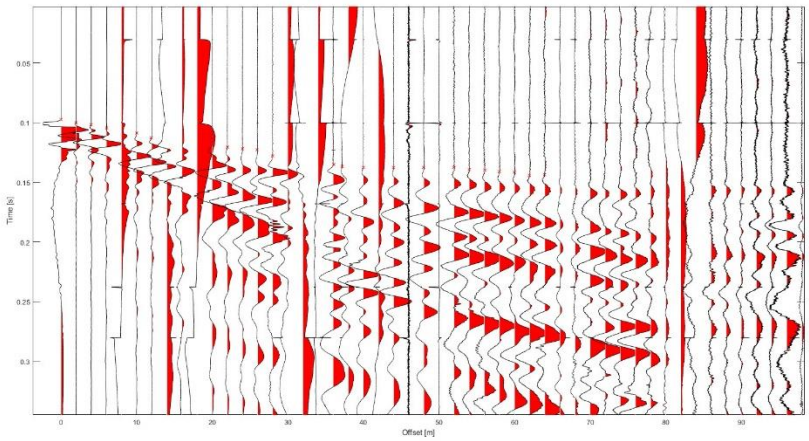

Figure 37 Example of Manual Travel Time picking for P-wave using Matlab from Seismic Survey 1 shot position at 0m, first geophone.

The entire process described was carried out across three Seismic Surveys, with certain considerations taken into account. As Seismic Surveys 1 and 2 are overlap at geophone position 25, consequently, also their travel times. Initially, they were considering as unique Seismic Survey to analysed and perform the first arrivals manual picking. Table 1 presents an overview of the data analysed, including the number of shots performed, their positions within the survey area (in meters), the tendency of time travel for the first and final picks obtained from the shot gathering, and the total measured time travel.

Table 1 Analysed Data for Seismic Survey 1, 2 and 3

Number of Matrix Matlab data	Seismic Survey 1	Seismic Survey 2	Seismic Survey 3
1	0 m	72 m	0 m
2	8 m	72 m	8 m
3	16 m	84 m	16 m
4	24 m	94 m	24 m
5	32 m	104 m	32 m
6	40 m	114 m	40 m
7	48 m	124 m	48 m
8	56 m	134 m	56 m
9	64 m	144 m	64 m
10	72 m	154 m	72 m
11	80 m	164 m	80 m
12	88 m	174 m	88 m
13	96 m	184 m	88m
14	104 m	194 m	104 m
15	112 m	204 m	112 m
16	120 m	214 m	120 m
17	128 m		128 m
18	136 m		136 m
19	142 m		142 m
Time travel measurements	901	698	1041

To perform inversion the open-source software C++/Python-based library pyGIMLi was implemented. It utilizes the shortest path algorithm, assuming energy travels as rays using a deterministic Gauss-Newton scheme. A forward operator simulates seismic ray tracing to compare the nonlinear relationship between P-wave model parameters (m) and observed first-time arrivals data (d). The goal is to minimize the dimensionless weighted χ^2 criterion, quantifying the misfit between the data produced by the model and measured, through iteration. Uncertainties associated with each pick and related to model constraints are also incorporated [24][25].

As the code was written in Python, it depends on the classical open-source packages as NumPy, Matplotlib. Meanwhile, the inversion scheme for the 2D tomography uses pyGIMLi library. The installation procedure and all necessary dependencies were found on the github page and performed through Anaconda environment [26][27]. Therefore, the input data was organized in a structured manner as ASCII format within a text file. Initially, the file should specify the number of shot/geophone points and their corresponding x and y coordinates. Following this, it should detail

the number of measurements, presenting the source and receiver positions alongside their associated picked travel times. It was performed for the three data seismic surveys, some considerations were taken, as topography influence in the ray tracing, x coordinates were corrected implemented the recorded GPS geophone position, therefore Seismic Survey 1 and 2 were analysed independently, spanning a total length of 133m and 129m, respectively, while Survey 3 covered a distance of 140m See Appendix A for further details.

After uploading the data, the Time Travel plots were generated for visualization (Figure 38, 39, and 40). To enable successful inversion during pre-processing, it was essential to exclude data associated with the shot position. Consequently, in the graphs, the travel time does not extend to 0.

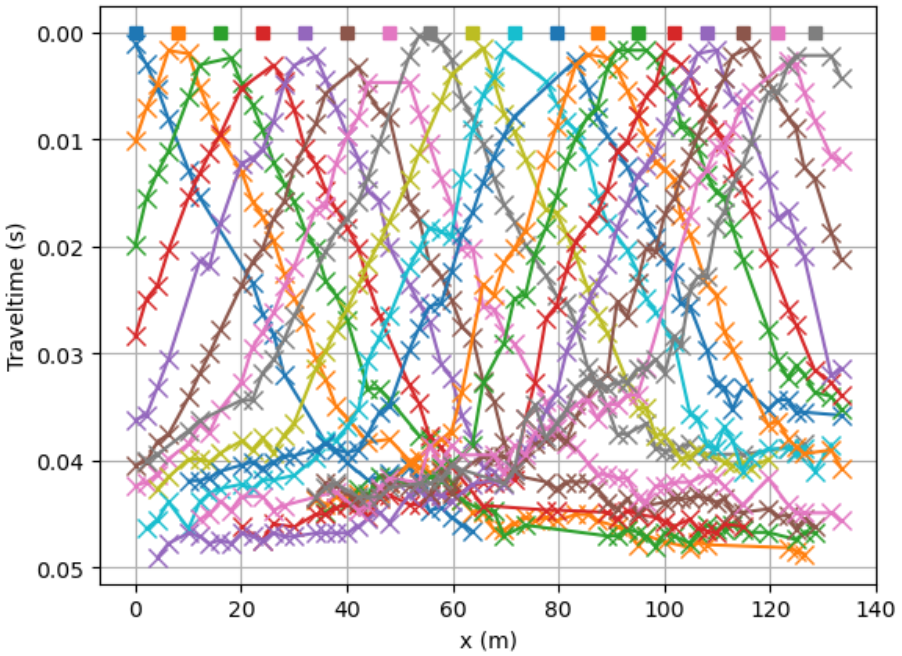

Figure 38 Travel Time from Seismic 1 survey performed at the edge of the Fourcare Dam

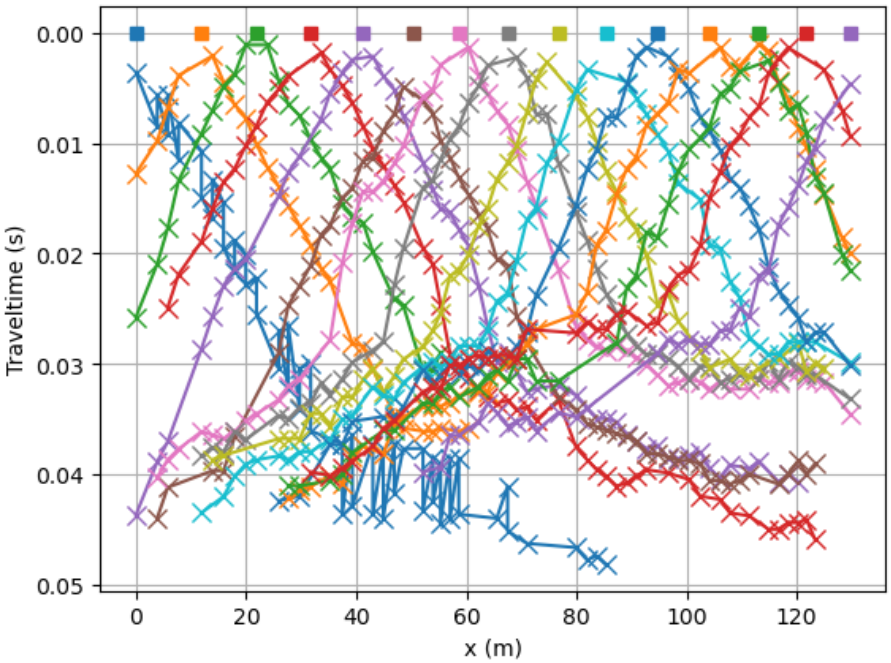

Figure 39 Travel Time from Seismic 2 survey performed at the edge of the Fourcare Dam

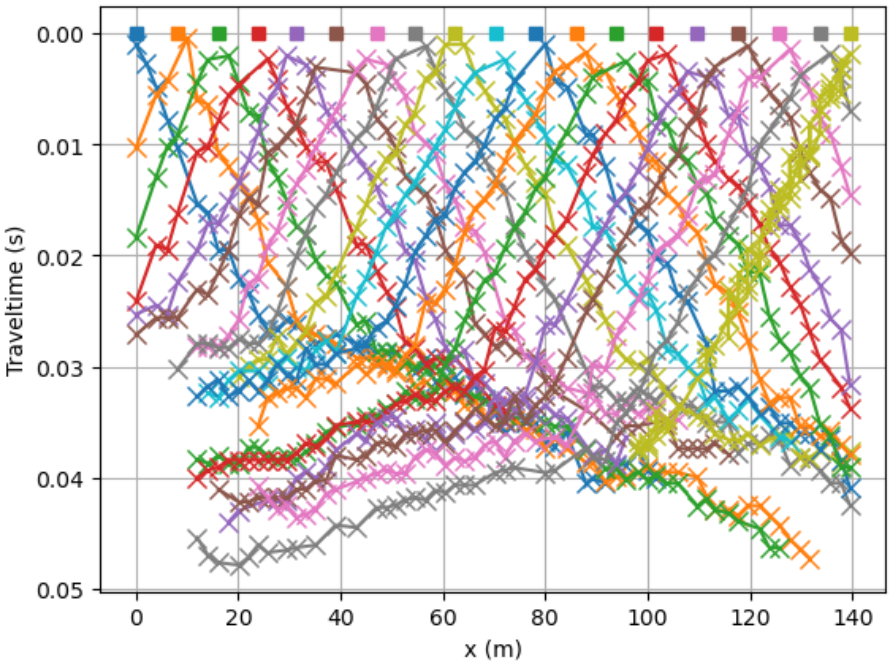

Figure 40 Travel Time from Seismic 3 survey performed at the edge of the Fourcare Dam

PyGIMLI initiates the inversion process by implementing a robust smoothing model (Eq. 8), initially enforcing significant constraints on the model parameters. Through iterative refinement, these constraints gradually diminish, allowing greater flexibility for parameter adjustments as data adjustments improve. Towards the latter stages of the process, smoothing in the z-direction may be reduced to accommodate velocity discontinuities at layer boundaries, a feature controlled by "Smoothing in z-direction". The selection of smoothing parameters may vary depending on the characteristics of the measured data. Default parameters are employed for the inversion procedure.

Initially, regions of interest are identified within the provided data, facilitating the creation of a forward mesh to simulate seismic wave propagation through the subsurface. This mesh is subsequently refined with the addition of five secondary nodes to enhance simulation accuracy. A gradient starting model is then generated, serving as an initial estimate for the inversion process. Subsequently, final inversion model is done, utilizing the specified forward operator, data, and model transformations. Employing χ^2 criterion (Eq. 4), its convergence is evaluated, and abort criteria is reached when it undergoes 2%. This criterion serves as a guide to ensure the accuracy and reliability of the inversion results. Velocities and ray-path models for each data survey can be observed (Figure 37, 38, 39, 40, 41, 42), only covered cells are shown by default [28].

The convergence of Seismic Tomography models for each Seismic Refracted Survey data was achieved after 6 iterations with a χ^2 of 1.05% for Seismic Survey 1, 8 iterations with a χ^2 of 1.42% for Seismic Survey 2, and finally 7 iterations with a χ^2 of 1.4% for Seismic Survey 3. In Seismic Survey 1, a notable increase in P-wave velocities to 3000 m/s is observed at a uniform depth of 20m, with Ray tracing extending uniformly to the same depth. Conversely, in Seismic Survey 2, this transition to 3000 m/s P-wave velocities occurs at a depth of 20m and gradually decreases to 10m along the survey, with Ray tracing covering depths up to 30m. Seismic Survey 3 exhibits an inclined stratum, with a shift to higher P-wave velocities of 3000 m/s at 10m depth, incrementing progressively to 20m along the survey. Ray tracing extends to a depth of 40m.

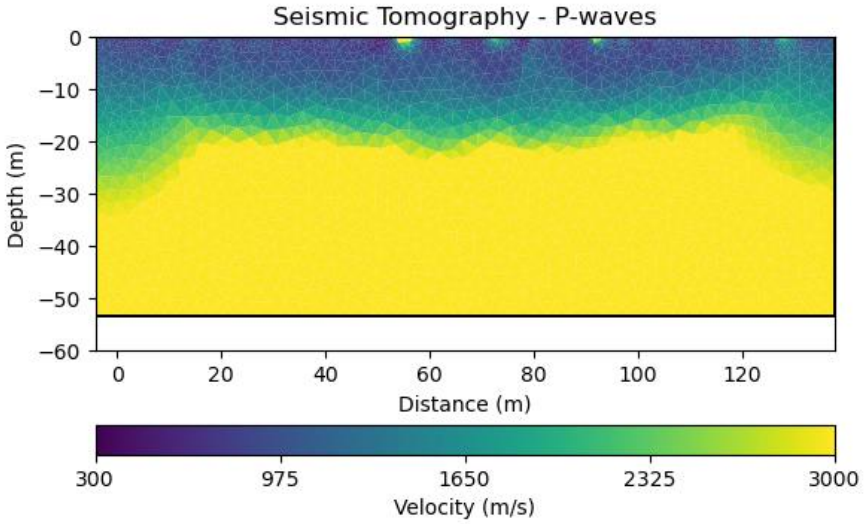

Figure 41 P-waves Velocities for Seismic 1 Survey

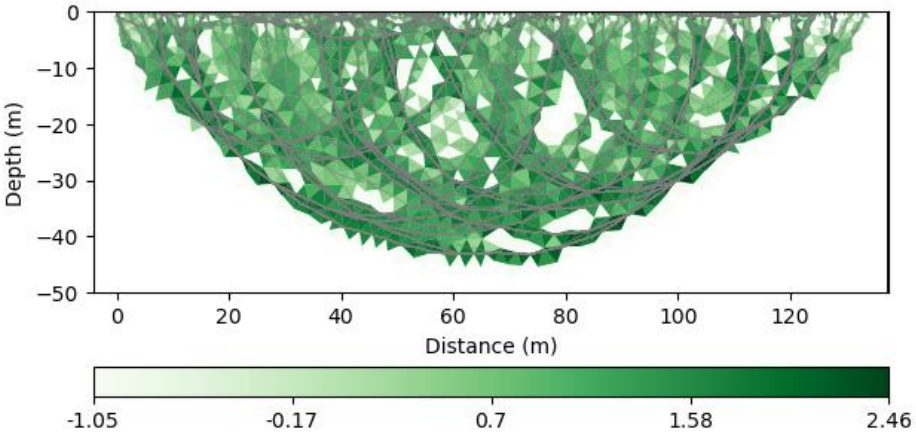

Figure 42 Ray-Coverage and Ray-Tracing for Seismic 1 Survey

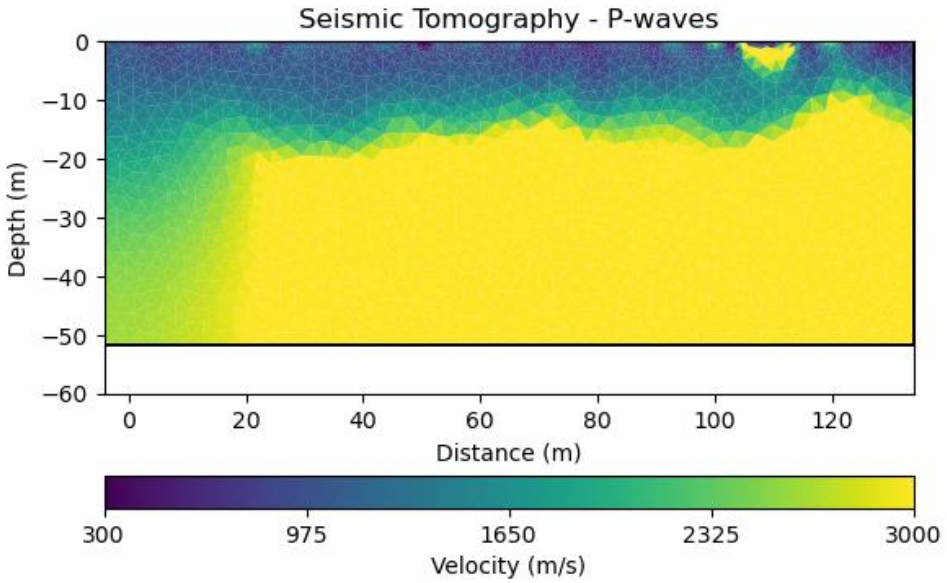

Figure 43 P-waves Velocities for Seismic 2 Survey

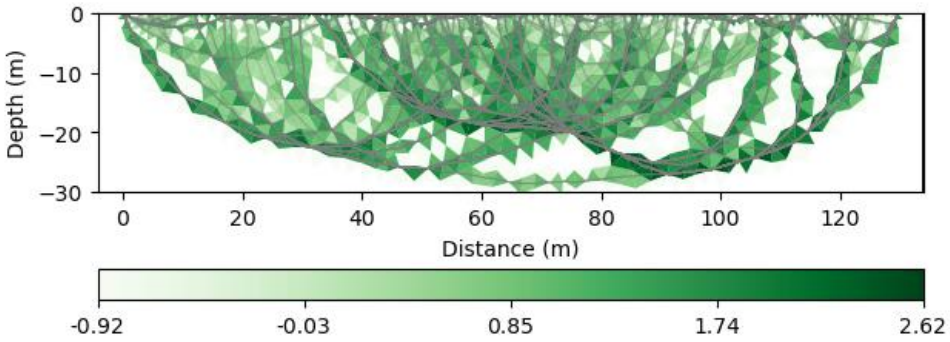

Figure 44 Ray-Coverage and Ray-Tracing for Seismic 2 Survey

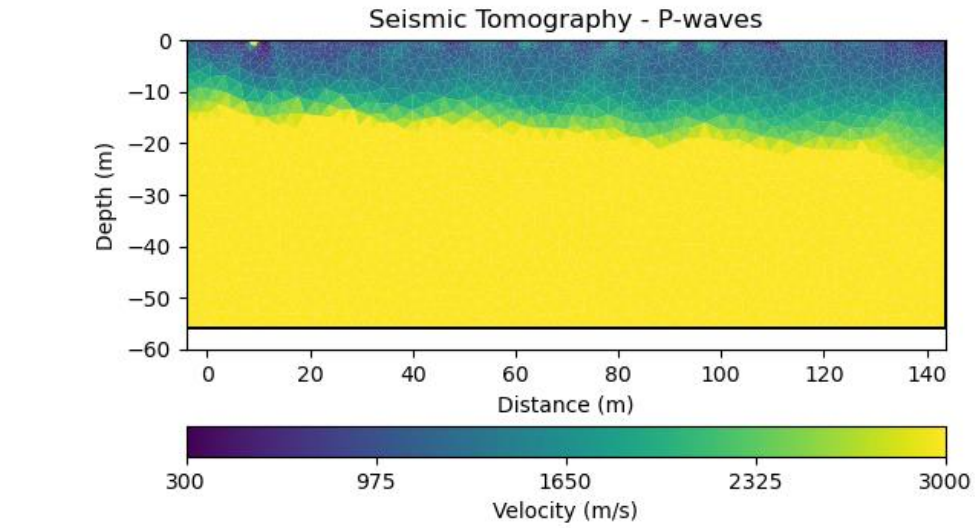

Figure 45 P-waves Velocities for Seismic 3 Survey

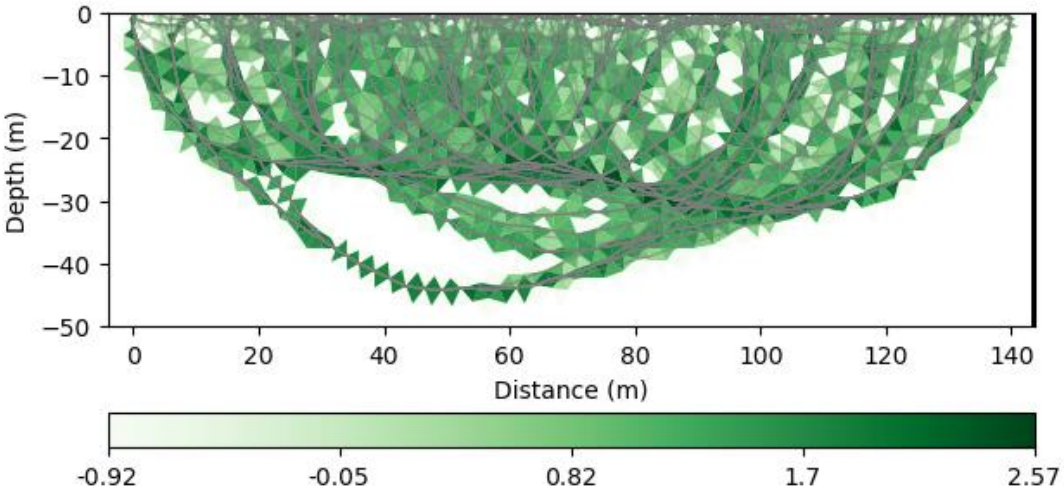

Figure 46 Ray-Coverage and Ray-Tracing for Seismic 3 Survey

4.1.5 Results

Finally, Velocities model and Ray Paths for each Seismic Refraction Survey (SRT) are overlapped (Figure 44, 45, 46), serving as a crucial tool to assess the reliability of the models. To enhance the identification of stratigraphic changes in P-wave velocities, the minimum and maximum observed data were adjusted.

In all three SRT models, three distinct strata are identifiable. The first layer, characterized by P-wave velocities around 1100 m/s, resides at the surface with an average thickness of approximately 10 meters. Notably, SRT 2 exhibits a decrease in depth along the survey, while SRT 3 demonstrates an opposing trend, with increasing depth along the survey path.

The second stratum, featuring P-wave velocities ranging between 1500 to 2000 m/s, is consistently observed at depths of 10 to 20 meters. While SRT 1 shows uniformity in this layer, SRT 2 and SRT 3 display variations mirroring the overlying strata. Finally, the last stratum is found at exceeding 20 meters depths, characterized by P-wave velocities of 3500 m/s.

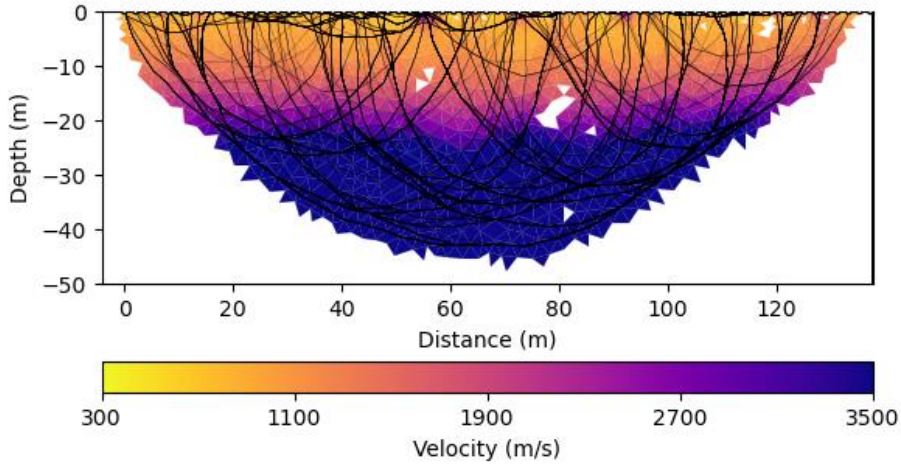

Figure 47 Ray-path and P-wave velocities model from Seismic 1 Survey

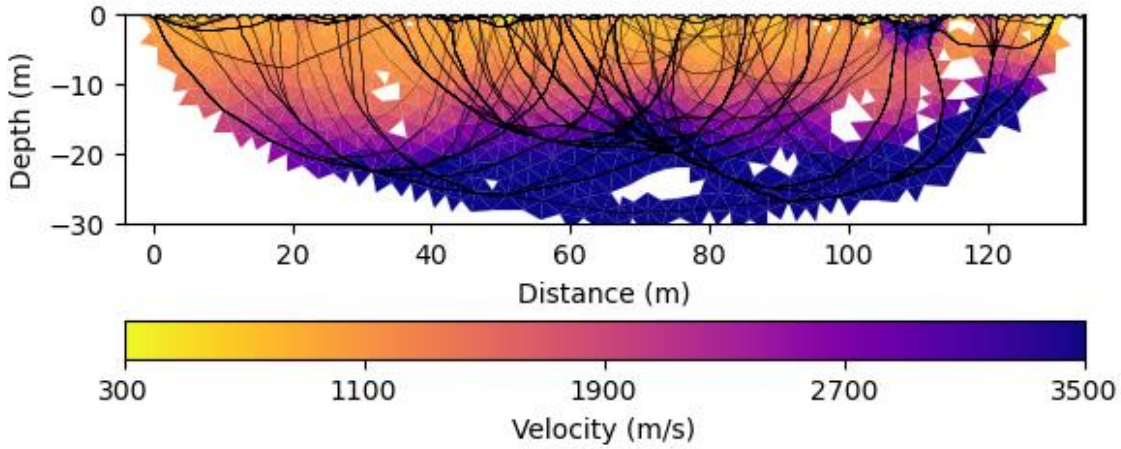

Figure 48 Ray-path and P-wave velocities model from Seismic 2 Survey

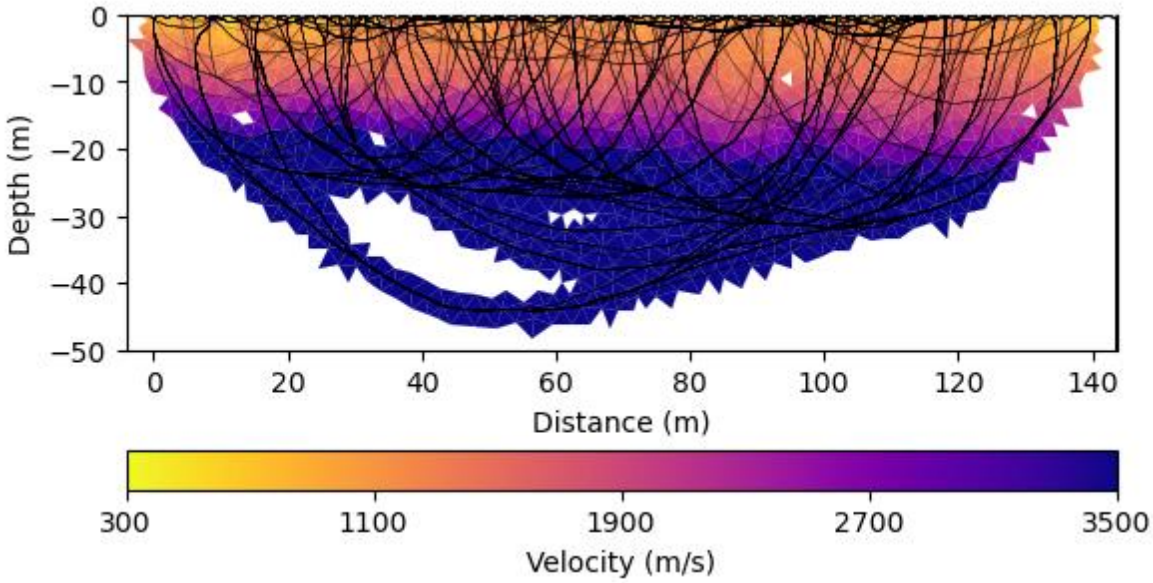

Figure 49 Ray-path and P-wave velocities model from Seismic 3 Survey

4.2 Surface Wave and VS velocities

As previously discussed, various types of surface waves exist, including Rayleigh, Love, Scholte, Lamb, and Stoneley waves. These waves travel along the free surface and exhibit an exponential decrease in amplitude with depth. Among them, Rayleigh waves are of particular importance, constituting approximately 67% of the elastic energy emitted by a seismic source.

Rayleigh waves, characterized by their high amplitude and low frequency, propagate primarily within a cylindrical region near the free surface. Consequently, their amplitudes at the surface are significantly greater than those of body waves. However, their amplitude diminishes rapidly with depth, with the value decreasing to less than 30% of its surface amplitude at a depth equivalent to one wavelength []

In heterogeneous media with spatially varying elastic moduli, Rayleigh wave packets become dispersive. Fourier analysis can decompose these wave packets into individual frequency components, each traveling at its characteristic phase velocity. The dispersion characteristic, depicted by the phase velocity versus frequency curve, provides valuable understanding of the medium's properties.

Techniques such as multichannel analysis of surface waves (MASW) utilize apparent Rayleigh phase velocity versus frequency curves to invert and derive shear-wave depth profiles. These profiles offer estimates of shear-wave speed in the shallow subsurface, which can be interpreted to assess physical properties like stiffness, liquefaction potential, and moisture content.

4.2.1 Introduction

As mentioned earlier, the velocity of the R-wave is affected by the elastic characteristics of the layers it encounters as it is primarily sensitive to S-wave velocities depth profile ($V_r \sim 0.92 V_s$ for a Poisson ratio of 0.25). This causes each frequency component of the R-wave to travel at its own specific phase velocity, a phenomenon referred to as geometric dispersion. Essentially, studying the R-wave's velocity across different frequencies, known as its dispersion characteristic, yields valuable information about the elastic properties of each layer within the system.

In a dispersive wave packet, each frequency component propagates at a distinct phase differing from the rest. In an idealized scenario where a source vibrates at a single frequency (Figure 47), the high-frequency signal within the lower frequency wave packet moves outward faster than the packet's envelope. Typically, dispersion causes distortion to occur in a wave packet as it traverses through a medium.

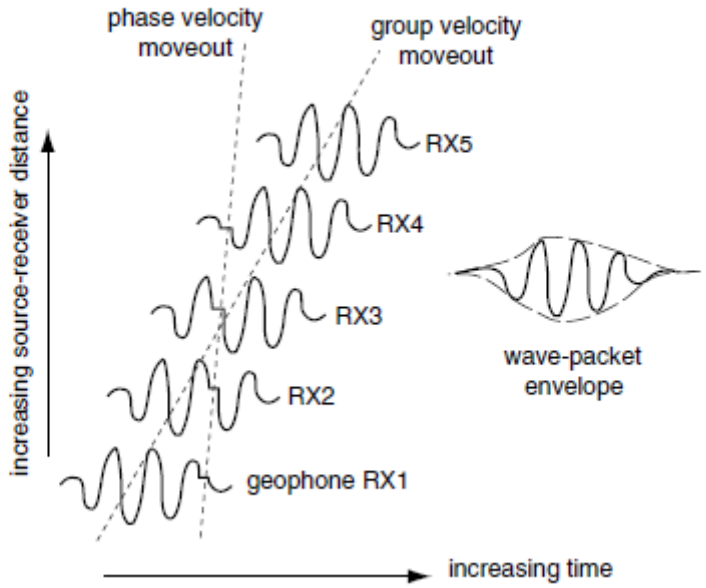

Figure 50 Scheme over a Dispersion Curve comparing phase and group velocities for Ideal Source

To consider Rayleigh-wave propagation over a multi-layer system, where Vs, Vp, density, and Poisson's ratio for ach N-1 layers and the terminating half space are known, it is possible to sketched how the dispersion characteristics Vph(f) is constructed. Firstly, it is necessary to introduce a pair of elastic-wave potentials (φ, ψ) called compressional potential and shear potential, respectively. Then, u_n and w_n (Eq 9) represents the horizontal and vertical displacement in the N-1 layer.

Equation 9

$$u_n = \frac{\partial \varphi_n}{\partial z} + \frac{\partial \psi_n}{\partial x}.$$

$$w_n = \frac{\partial \varphi_n}{\partial z} - \frac{\partial \psi_n}{\partial x}$$

Equation 10

$$\varphi_n = U_{Pn} \exp(r_n z) + D_{pn} exp(-r_n z)$$
$$\psi_n = U_{Sn} \exp(s_n z) + D_{Sn} exp(-s_n z)$$

Therefore, the coefficients U_{Pn}, U_{Sn} correspond to the up-going waves, while D_{pn}, D_{Sn} to the down going waves. Meanwhile, r_n and s_n represents composite wavenumbers. For P-wave and S-wave with an angular frequency ω propagating over N-1 layers (Eq 10) and k_{ph}^2 (Eq 11), the wavenumber ($f = \omega/2\pi$) propagates with a velocity Vph.

Equation 11

$$r_n^2 = k_{ph}^2 - k_{pn}^2$$
$$s_n^2 = k_{ph}^2 - k_{sn}^2$$

The determination of unknown coefficients involves the application of boundary conditions. These include the continuity of normal and shear stress across layer interfaces, as well as the continuity of horizontal and vertical displacement across these interfaces. Additionally, the boundary conditions entail the vanishing of normal and shear stress at the free surface and the absence of up-going waves.

These conditions lead to a linear relationship between surface displacement and bottom-layer elastic wave potential coefficients. This relationship is described through a matrix R of 2x2 dimension, which incorporates the phase velocity Vph and the wave frequency f. By rearranging this relationship, a non-trivial solution for the surface displacements is obtained, represented ($g(Vph, f)$=0) known as Rayleigh secular equation.

Various values of Vph satisfying this condition for a given frequency f constitute a range of dispersion characteristics called modes. These modes can be categorized into fundamental modes, which exist for all frequencies, and higher modes with higher phase velocities. Higher modes only exist above a cutoff frequency that depends on the specific mode.

4.2.2 Working Principle

Multi-Channel Analysis of Surface Waves (MASW) involves several key steps: acquiring high-frequency broad-band Rayleigh waves, extracting dispersion curves, and utilizing inversion techniques to derive near-surface S-wave velocities [29]. In a typical seismic survey (see Figure 30), a shot gathering yields data that undergoes Fourier transformation, resulting in a frequency domain wavefield, u, where ω represents angular frequency, A(x,ω) signifies the amplitude spectrum, and Φ(ω) = ω/Vph(ω), with Vph denoting the surface wave phase velocity at frequency ω (Equation 12).

Equation 12

$$u(x, \omega) = A(x, \omega) Exp| - i\Phi(\omega)x|$$

After applying linear transformation and normalization to u, a function v(x,ϕ) is defined and integrated over an offset. Notably, peaks in v(x,ϕ) occur at values where ϕ = Φ = ω/Vph(ω), thus determining Vph(ω). These peak values are visually represented in a 2D counter plot of v(x,ϕ) or (f, Vph) commonly known as a dispersion image and from the observation of fundamental and possible higher-modes, the inverse problem is solved, which includes back-calculation of Vs(z) depth profile though a misfit function.

4.2.3 Data processing

As previously described, MASW (Multichannel Analysis of Surface Waves), uses seismic data collected from shot gathers (Section 4.1.3) to extract dispersion curves, particularly those associated with Rayleigh waves. Then they are analysed and interpreted to estimate the shear-wave velocity (Vs) profile of the near surface.

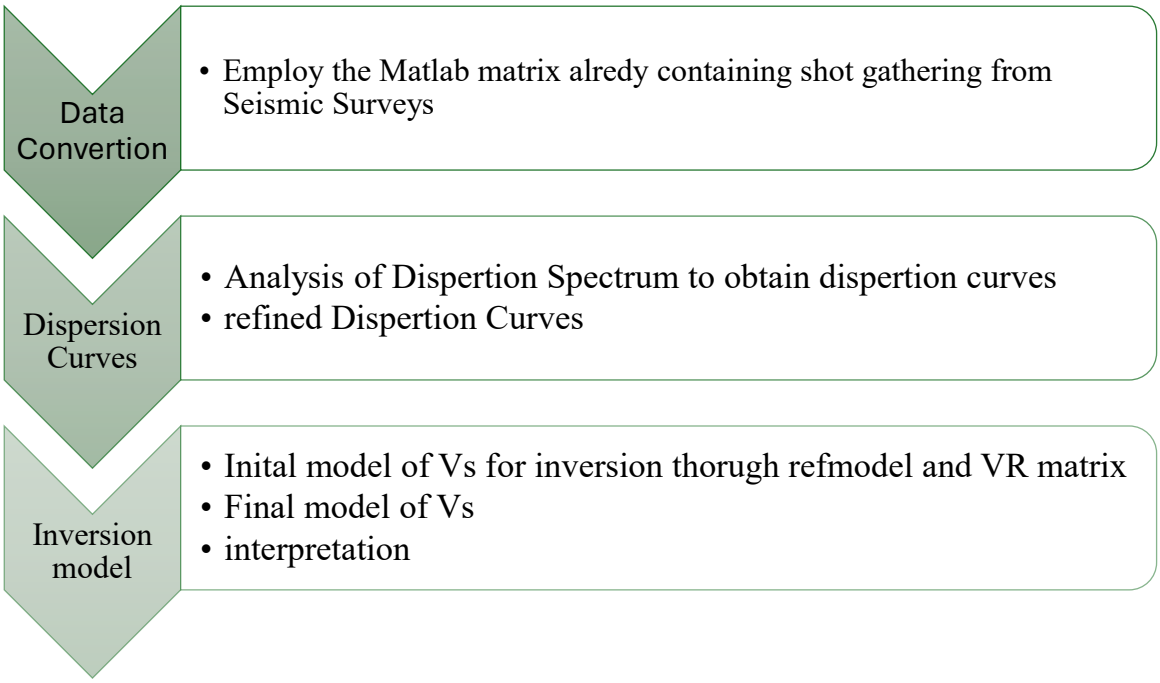

Figure 51 Scheme Data processing for MASW.

The Dispersion Curves (DC) were derived from the corrected Matlab matrix obtained from shot gathering data collected during the previous S1, S2, and S3 Seismic Surveys. Initially, a Matlab Script was employed to compute the frequency-phase velocities, saved as spectra, and later used for Dispersion Curve picking. This necessitated the inclusion of all shot gathering data and the arrangement of geophone receiver coordinates into a matrix, with corresponding East and North coordinates for each Survey.

The process involved setting initial parameters such as spatial window size, step size, and maximum number of shots for spectral stacking during DC computation. Additionally, minimum, and maximum frequencies, as well as minimum and maximum phase velocities, were defined as vectors for estimated DC velocities. A spatial window of 16 tracers with a step of one tracer was employed, with a maximum of 5 shots considered. Frequencies ranged from 15 to 60 Hz, and phase velocities ranged from 200 to 3000 m/s.

Through iterations over the shot gatherings and utilizing geometry information, frequency spectra were obtained via Fourier Transformation within the defined spatial window. All spectra were saved, and stacked spectra for each window were generated. Dispersion curves, representing Rayleigh waves' fundamental modes, were automatically identified. Further refinement was achieved through manual picking using he ginput function, which allowed for the selection of the region of interest by defining a rectangular area through the right-click selection of vertices (Figure 49). Finally, cleaned Dispersion curves were plotted and saved as a Matlab matrix.

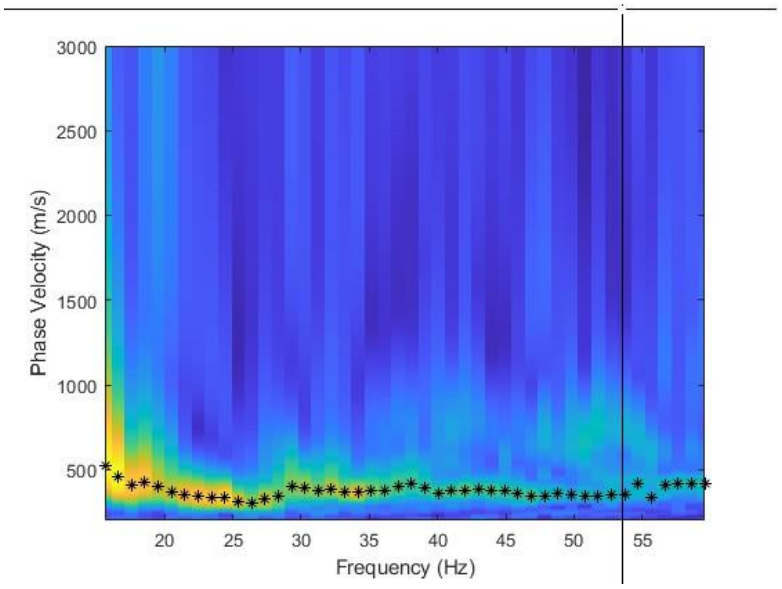

Figure 52 Manual picking over Dispersion Spectrum to increase accuracy of the Dispersion Curves obtained from Shot gathering recorded at Seismic Survey 1.

To initiate the inversion process, an initial model was formulated based on a reference model and Rayleigh wave obtained from each Seismic Survey data. The reference model was constructed using a Matlab matrix structured such that the number of columns corresponds to the number of previously obtained Dispersion curves. The initial model consists of the assumed number of layers, followed by the coordinates of the Dispersion curves, default files indicating layer properties, such as density, Poisson ratios, and thickness, as well as the shear wave velocities (Vs) for the assumed layers. For all data, were consider an Initial model of five layers, with density values of 1800, 1900, 2000, 2200, 2400, and 2600 kg/m³. A Poisson ratio of 0.25 was utilized, with each layer having a thickness of 5 meters. The assumed Vs values for the layers were 300, 500, 700, 900, 1500, and 2000 m/s.

Subsequently, the VR matrix for the initial model was organized into four columns. The first column denotes the number of Dispersion Curves, followed by a column specifying their frequencies and Rayleigh wave properties, finally un uncertainty of 50 m/s was assumed (See Appendix B). Matrices dimensions of Initial Vs Models and Number of Dispersive Curve for each Survey data were summarized at Table 2.

Table 2 Matrices Dimension for Initial Vs Model and Number of Dispersive curves for Each Survey data

	Seismic Survey 1	Seismic Survey 2	Seismic Survey 3
N° Dispersive Curve	28	28	28
Reference Model	28 x 53	28 x 45	28 x 57
Vr	1072 x 4	384 x 4	1458 x 4

To obtain the final Vs model, an iterative process refines the initial Vs model using experimental dispersion curves provided by the VR matrix. This process iteratively adjusts the initial shear wave velocity (Vs) model based on input variables, including experimental dispersion curves, the initial Vs model, and any a priori information on model parameters.

During each iteration, the initial model undergoes updates based on observed dispersion curves and constraints derived from the a priori model and depths. The output of each iteration comprises the updated Vs model along with its theoretical dispersion curves. Covariance matrices and regularization matrices are employed to effectively manage constraints throughout the process. After numerous iterations, the process converges towards a final Vs model, providing a significantly improved estimation of subsurface shear wave velocities derived from seismic data measured by its misfit function. The final Vs models for the three initial Vs models were obtained after 39 iterations, considering 50 m lateral, and vertical constrains along the thickness, velocities, and depth.

Dispersive curves as Normalised residuals and last iteration parameter from Final Vs Models are followed reported (Figure 50, 51, 52, 53, 54, 55).

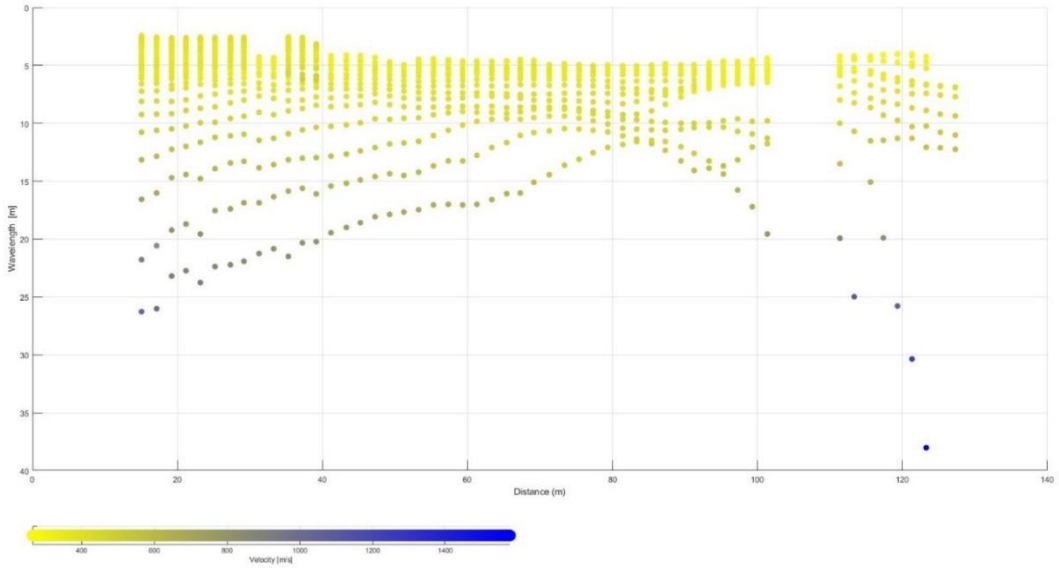

Figure 53 Dispersion curve for Final Model Vs from Seismic Survey 1 data.

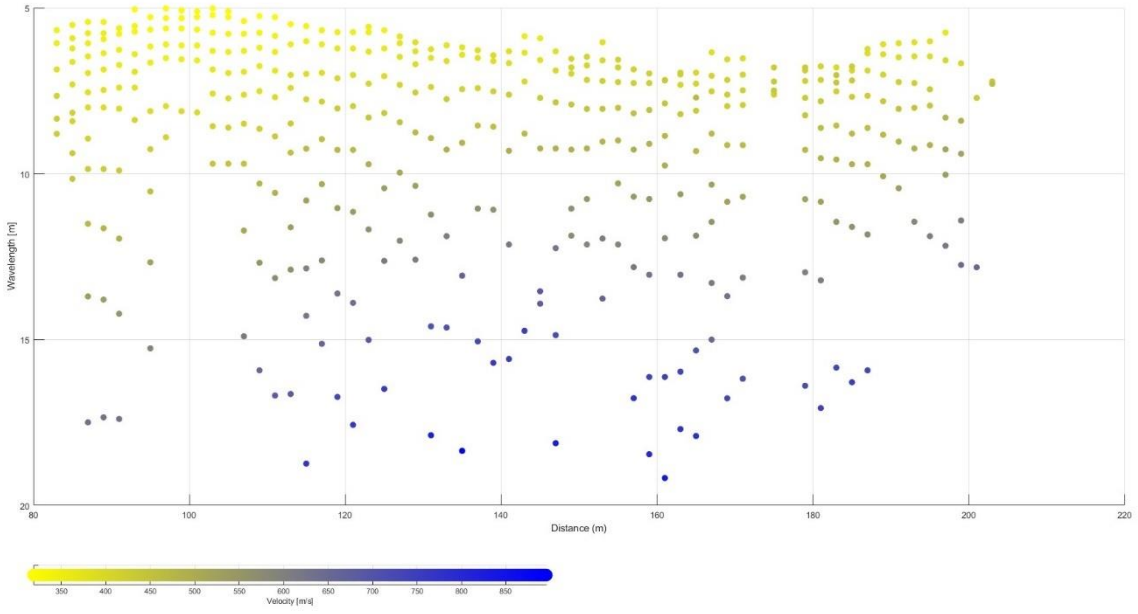

Figure 54 Dispersion Curve for Final Model Vs from Seismic Survey 2 data.

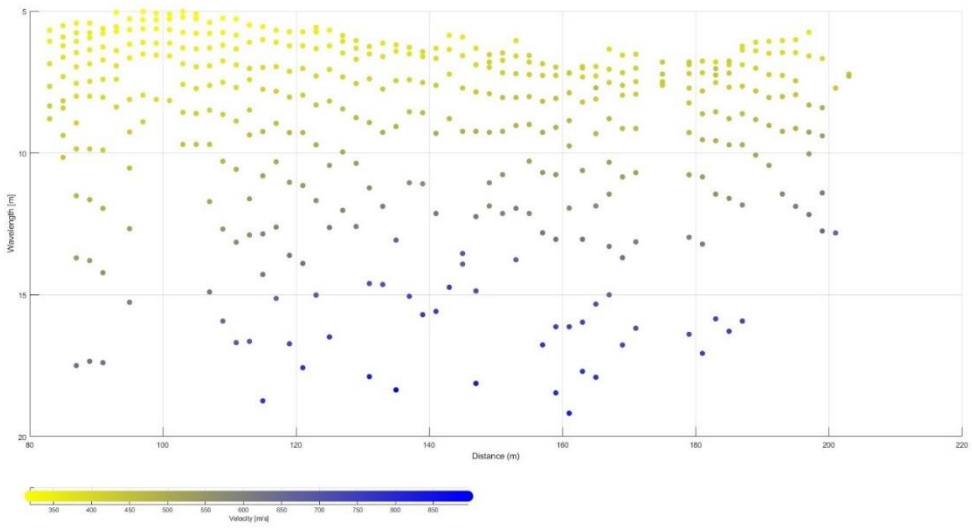

Figure 55 Dispersion Curve for Final Model Vs from Seismic 3 data.

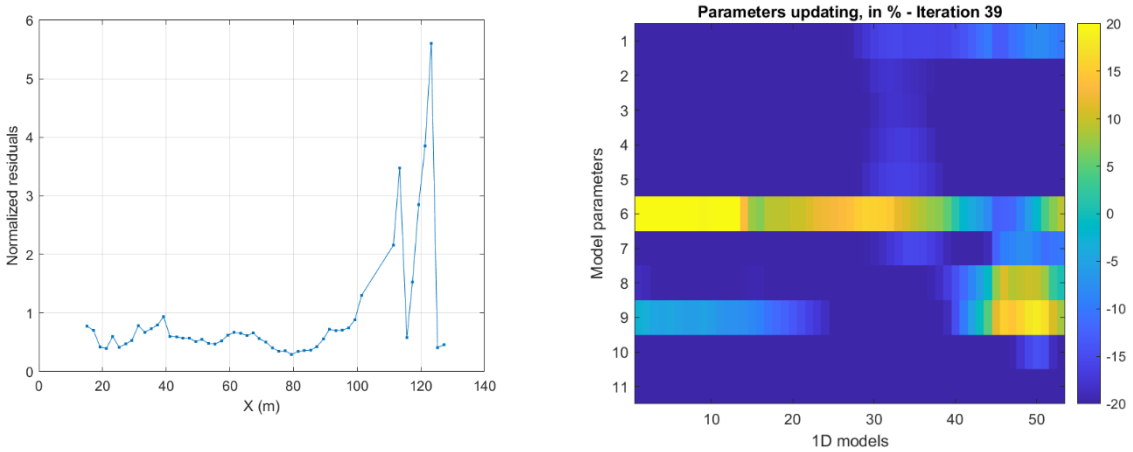

Figure 56 (a) Normalized residual and (b) Last parameter iteration for Final Vs Model from Seismic 1 data.

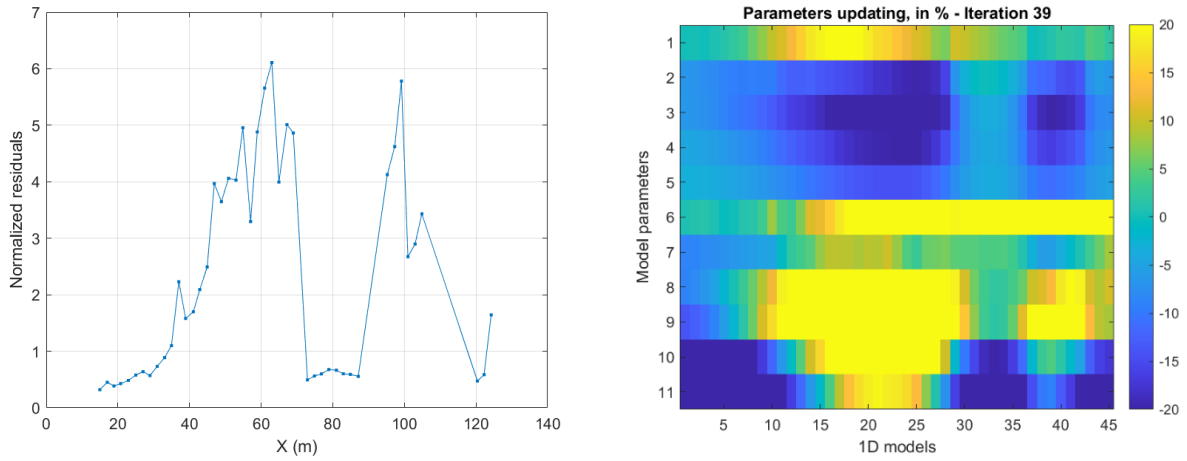

Figure 57 (a) Normalized residual and (b) Last parameter iteration for Final Vs Model from Seismic 2 data.

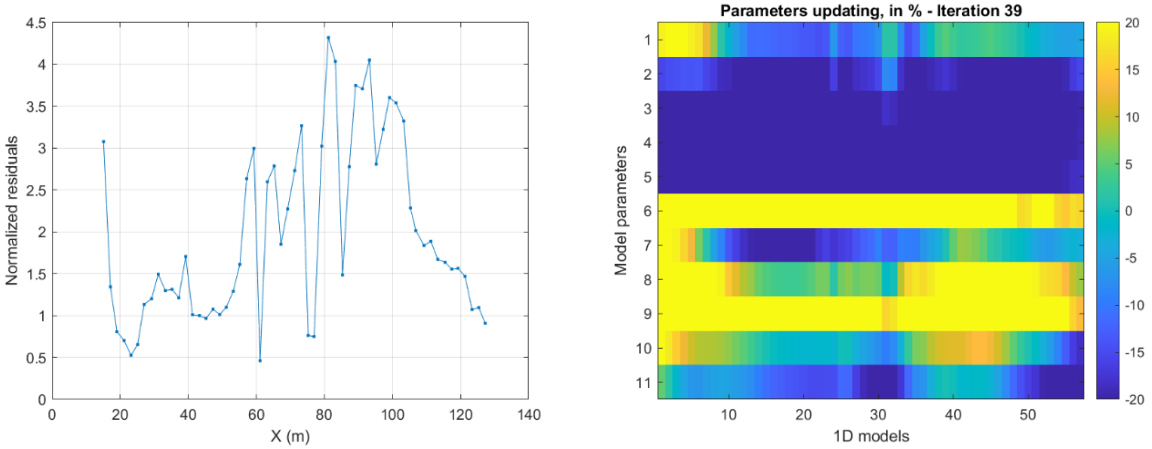

Figure 58 (a) Normalized residual and (b) Last parameter iteration for Final Vs Model from Seismic 3 data.

4.2.4 Results

For the Vs models derived from Seismic 1 and 3, the depth coverage extends up to 20 meters, whereas the Seismic 2 Vs model reaches a depth of 25 meters. In all models, an initial layer of 5 meters thickness with a Vs velocity of 500 m/s is consistently observed. However, due to the energy emitted by the seismic source, further discretization beyond this depth is not feasible.

Typically, one would anticipate an increase in Vs velocities with depth, reflecting the compaction and consolidation of geological materials. Nevertheless, this expected trend is not observed in the Vs model for Seismic 1. Instead, a lateral variation is evident between offset distances of 70 to 90 meters, where low Vs velocities of 600 m/s are observed at greater depths. Similarly, the Vs model derived from Seismic 2 also exhibits a lateral variation, with low velocities observed at offset distances of 0 to 30 meters and again at 70 to 90 meters.

The white regions observed in the models indicate areas where dispersion curve data is lacking. These findings provide valuable insights into the subsurface geological characteristics, contributing to a better understanding of the seismic response in the study area.

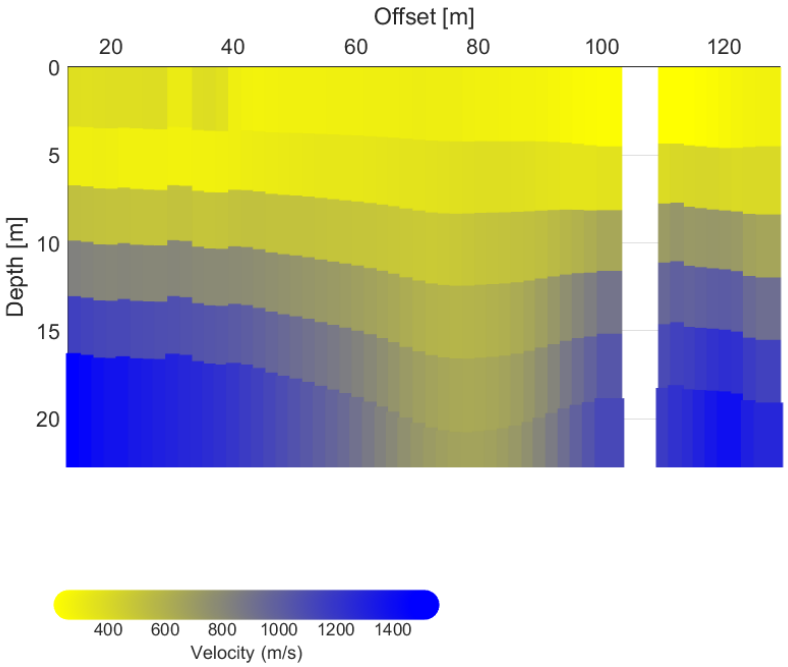

Figure 59 Final Model Vs velocities for Seismic 1

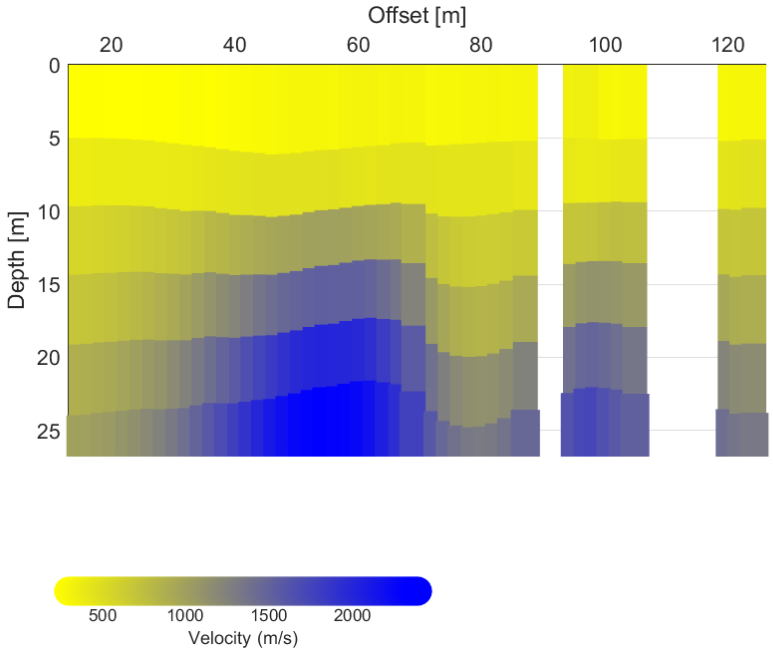

Figure 60 Final Model Vs velocities for Seismic 2

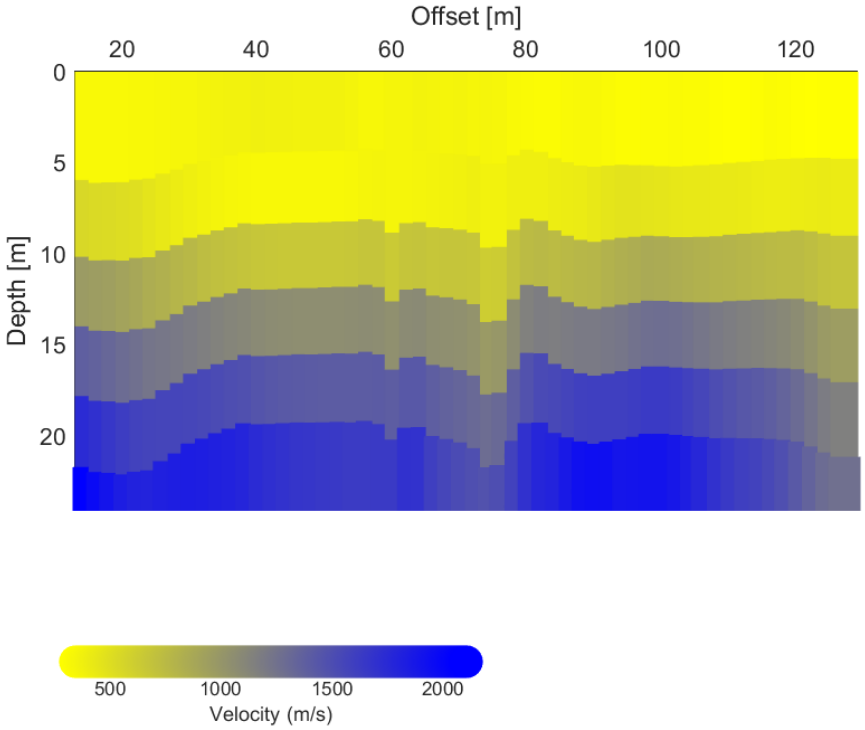

Figure 61 Final Model Vs velocities for Seismic 3

5 Geotechnical Parameters

5.1 Introduction

How it was already introduced, when a seismic source emits energy it creates elastic strain, initiating the propagation of seismic waves, which velocities intricately linked to the elastic moduli and densities of the materials they traverse. This fundamental relationship between seismic waves and elastic properties is crucial to understand spatially distribution of soil mechanical properties.

5.2 Working Principle

Specifically, P-waves and S-waves provide valuable information about the subsurface's mechanical properties, as Young's modulus E [N/m2], which is a measure of the longitudinal stress to the longitudinal strain, Poisson's ratio σ, a dimensionless measurement of the transverse strain to longitudinal strain, shear modulus μ [N/m2], which measures the tangential stress to tangential strain, or shear stiffness and bulk modulus k [N/m2], a measure of the volume change in response to a change in hydrostatic pressure, or compressibility. Those relationships are highlighted in (Eq. 13, 14 and 15).

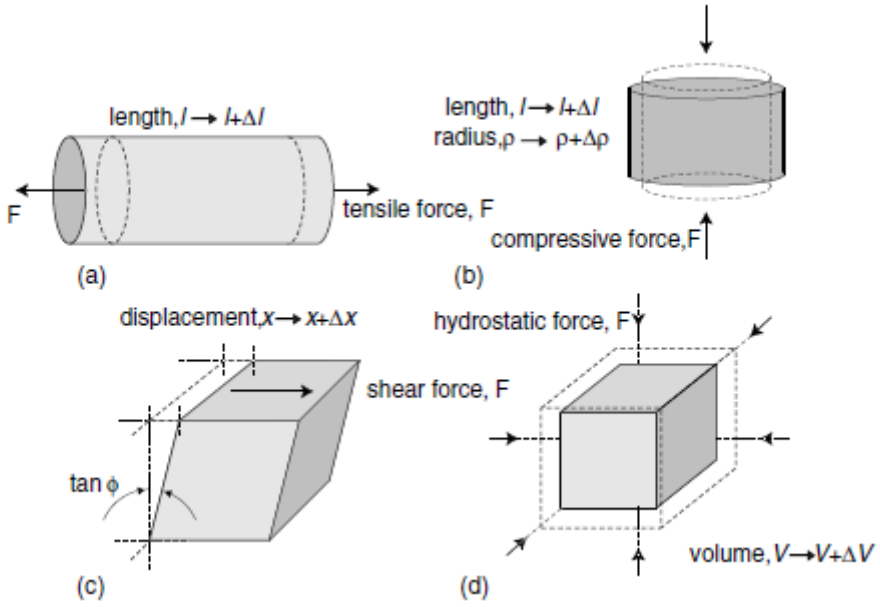

Figure 62 Definition of Elastic Parameters (a) Young Modulus (b) Poisson´s ratio (c) Shear Modulus (Mark E. Everett (2013). Near Surface Applied Geophysics. Cambridge University Press)

Equation 13

$$Vp = \sqrt{\frac{k + 4\mu/3}{\rho}} = \sqrt{\frac{(1-\sigma)E}{(1+\sigma)(1-2\sigma)\rho}}$$

Equation 14

$$Vs = \sqrt{\frac{\mu}{\rho}} = \sqrt{\frac{E}{(1+\sigma)2\rho}}$$

Equation 15

$$\frac{Vp}{Vs} = \frac{\sqrt{2(1-\sigma)}}{1-\sigma}$$

5.3 Data Processing

Implementing P-wave and S-wave obtained from the Seismic Surveys performed, as final step, it is possible evaluate the mechanical properties of the site, and moreover the earth dam (Figure 60).

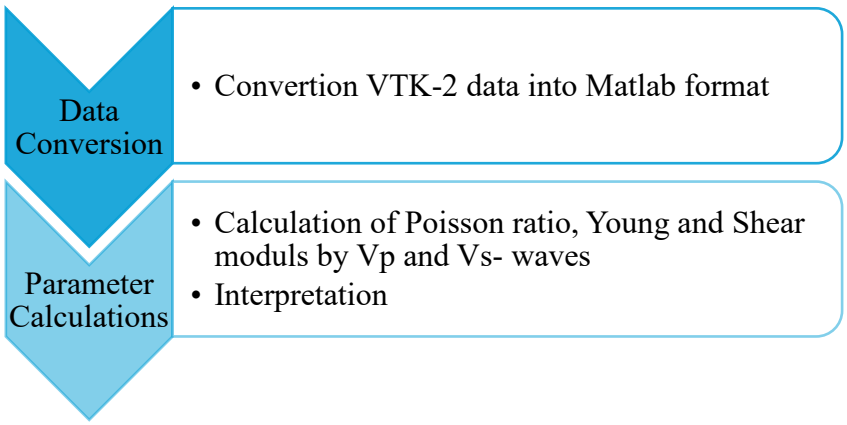

Figure 63 Scheme Data Processing for Poisson ratio, Young and Shear Modulus by Vp and Vs-wave.

As P-waves from Seismic Refraction Tomography were obtaining implementing the open-source software C++/Python-based library pyGIMLi, it was necessary firstly to convert the VTK-2 data

into a Matlab format. Meanwhile S-waves obtained from each Final Vs model performed, are found in ASCII. Together were implementing to calculate Poisson's ratio, Shear and Young modulus (Eq. 13, 14 and 15). Using Partial Differential Equations to smoother the visualization.

5.4 Results

The final plots depicting Mechanical Parameters derived from P-wave and S-wave data for each Seismic Survey are shown (Figure 61, 62, and 63). Notably, higher Poisson ratio values exceeding 0.4 are observed, which may indicate the presence of saturated clay material. In Seismic Survey 1, these elevated values are concentrated as a core at the midpoint of the offset distance and prevail predominantly in the upper layer. For Seismic Survey 2, the Poisson ratio values are primarily concentrated in the upper layer, extending notably beyond the midpoint. However, in the initial segment, a lower range of Poisson ratio values (0.2 - 0.3) is observed, might indicating rock material. Finally, in Seismic Survey data 3, higher Poisson ratio values are noticeable in both the upper and lower layers at the initial segment of the offset distance. Nonetheless, in the latter part of the survey, lower values corresponding to 0.2-0.3 are observed [30][31].

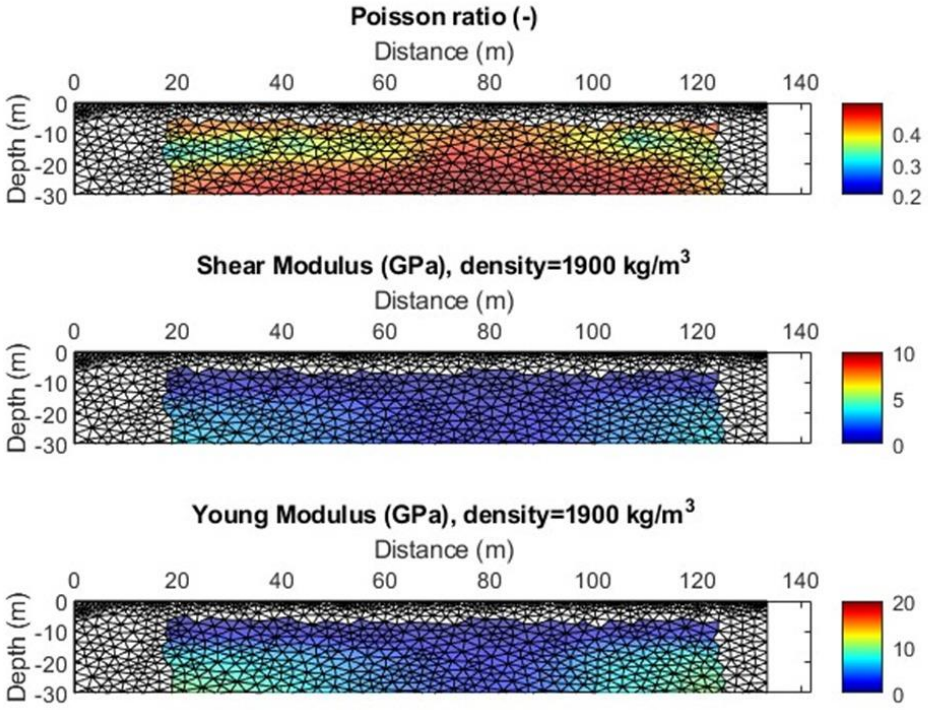

Figure 64 Geotechnical Parameters obtained through P-waves and S-waves from Seismic Survey 1 data.

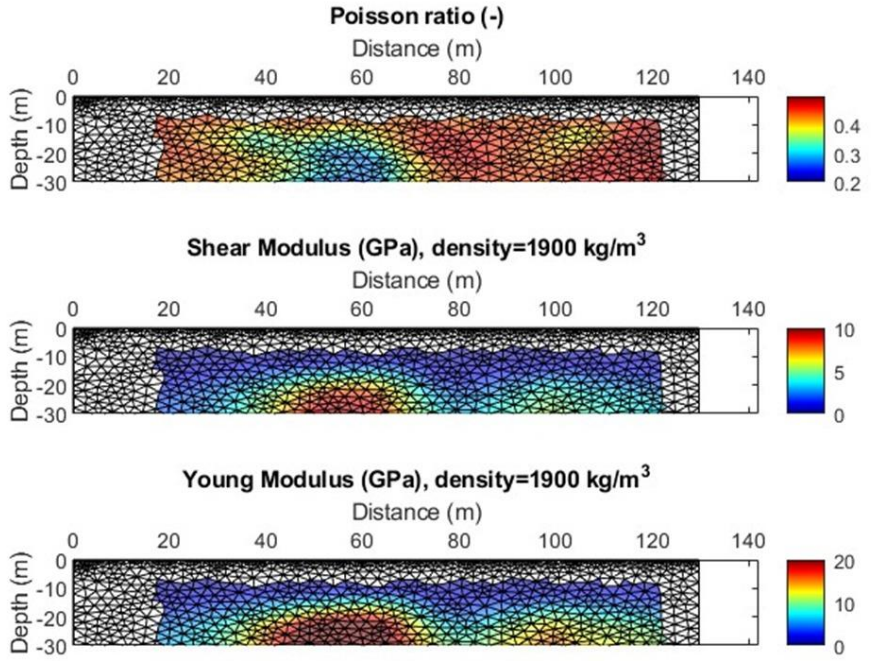

Figure 65 Geotechnical Parameters obtained through P-waves and S-waves from Seismic Survey 2 data.

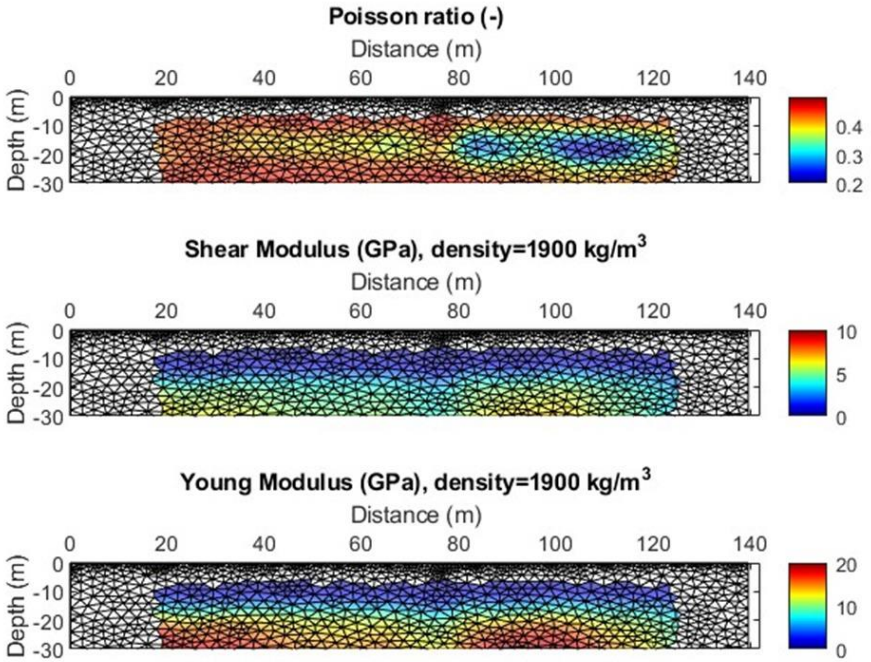

Figure 66 Geotechnical Parameters obtained through P-waves and S-waves from Seismic Survey 3 data.

6 Discussion

As it was described at the Site Investigation, mostly of the body embarkment was built using site materials and posed over a compacted layer. At the same 11.5 m depth, the drainage system is found composed of gravel site material. For the impermeabilize system, it was built by 20 -30 cm of site fine material over the impermeable layer and additionally, on the top part of the shore bathed by the water, the stone material was filled in with finer material to naturalize the appearance of the shores as much as possible. Later, the formation of the dam embankment proceeded by placing the sifted and selected material resulting from the excavations carried out for the construction of the reservoir until reach the maximum height of 14.90m, therefore the crest is found at 2326 l m.s.m. The material was placed in successive layers approximately 30-50 cm thickness, properly compacted. Finally, the slope over the embarkment is approximately of 20-22°, meanwhile, the downstream side of the artificial dam has an average slope of approximately 25°.

How it was highlighted at the results P-waves from Seismic Refraction Tomography for the three Seismic Surveys performed, the second stratum is observed at 10 m depth with P-waves values of 1500 to 2000 m/s, which could correspond to the layer body embarkment is placed. Meanwhile, for S-waves from Final Vs models, also the change of velocities is observed at 10m depth to 1000 m/s, except for the horizontal variations remarked with lower values of 600 m/s, which are shown at Poisson ratios. As it was seen, they were higher values that possible indicates, that in reality might be occurring a degradation of the material, because in the case of being saturation, S-wave should not be affected, only P-waves, as it takes into account water content.

7 Conclusion

For a complaint understanding and completely discard of possible saturation zones, it would be convenient to perform all the geophysics analyses with Piezometric data, as ERT can highlight possible filtration, but they cannot be completely assumed as true. Produce transversal sections over the dam body where piezometric are found, would be incredibly helpful to see where water table is found and if it corresponds to ERT measured data obtained.

However, for this Thesis, geophysics techniques as SRT, ERT and S-waves Ansys from Rayleigh waves shown to be a powerful tool to evaluate dam stability without compromise penetration over the hydraulic structure and more over to completely characterize over larger areas, a great restriction found by typical measurements monitoring earth dams. Therefore, it is highly recommended the use of geophysics surveys to complete the typical monitoring routine.

References

1] Deangeli, C., Giani, G.P., Chiaia, B., & Fantilli, A.P. (Politecnico di Torino, Turin, Italy; State University of Milan, Milan, Italy). "Dam failure."

2] World Commission on Dams. (2000). "Dams and developments: A new framework for decision making."

3] Dagnelli, C., Giani, G.P., Chiaia, B., & Fantilli, A.P. "Chapter 1, Dam Classification." In D. de Wrachien & S. Msmbretti (Eds.), *Dam-break problems, solutions and Case studies*. WIR Press Southampton, Boston. 2009.

4] Tahmiscioglu, M. Sait, Naul, Nermin, Ekmekci, Fatih, & Durmus, Nurcan. "Positive and negative impacts of dams on the environment." In *Integral Congress on river basin management*.

5] Schmutz, S., & Sendzimir, J. "Riverine Ecosystem Management." In J. Huisman (Ed.), *Science for Governing Towards a Sustainable Future* (Aquatic Ecological Series, Volume 8). Institute for Biodiversity and Ecosystem Dynamics, University of Amsterdam, Amsterdam, The Netherlands.

6] Fantilli, A.P., De Biagi, V., & Veylon, G. "A protocol to assess the seismic criticality of existing small concrete dams." *Barbara Frigo*. DOI: 10.1080/15732479.2017.1402066

7] Brewitt, P.K., Chelsea L.M., & Colwyn. "Little dams, big problems: The legal and policy issues of non-jurisdictional dams." DOI: 10.1002/wat2.1393

8] Mouvet, L. (Laboratory of Hydraulic Constructions, Swiss Federal Institute of Technology Lausanne, Switzerland), Muller, R.W., & Pougatsch, H. (Federal Office for Water and Geology, Biel/Bienne, Switzerland). "Structural Safety of dams, according to the new Swiss legislation."

9] Pisaniello, J.D., Dam, T.T., & Tingey-Holyoak, J.L. "International dam safety assurance policy benchmarks to avoid dam failure flood disaster in developing countries." DOI: 10.1016/j.jhydrol.2015.09.077

10] The World Bank. "Safety of Dams and Downstream Communities." *Small Dam Safety, technical note 4*.

11] Repubblica Italiana, R.I. (2014). "Norme tecniche per la progettazione e la costruzione degli sbarramenti di ritenuta (dighe e traverse)." *D.M. I.I.T.T. 26/06/14*. *Gazzetta Ufficiale della Repubblica Italiana*, 156, 1–35 (in Italian).

12] Marnezy, A. (2008). "Alpine dams." *Journal of Alpine Research | Revue de géographie alpine*, 96-1. DOI: https://doi.org/10.4000/rga.430.

13] Rixen, C., Teich, M., Lardelli, C., Gallati, D., Pohl, M., et al. (2023). "Winter Tourism and Climate Change in the Alps: An assessment of Resource Consumption, Snow Reliability, and Future Snowmaking Potential." *Mountain Research and Development (MRD)*, 31(3), 229-236. DOI: 10.1659/MRD-JOURNAL-D-10-00112.1

14] Bacchiocchi, S.C., Zerbe, S., Cavieres, L.A., & Wellstein, C. (2019). "Impact of ski piste management on mountain grassland ecosystem in the Southern Alps." *Science of the Total Environment*. DOI: 10.1016/j.scitotenv.2019.02.086

15] IPCC. (2023). *Climate Change 2023: Synthesis Report*. Contribution of Working Groups I, II and III to the Sixth Assessment Report of the Intergovernmental Panel on Climate Change. IPCC, Geneva, Switzerland. DOI: 10.59327/IPCC/AR6-9789291691647

16] Legambiente. (2023). *Neve Diversa, Il turismo invernale nell'era della crisi climatica*. In V. Bonardo (Ed.). Italy: Legambiente.

17]

18] Foster, M., Fell, R., & Spannagle, M. (2000). "The statistics of embankment dam failures and accidents." *Canadian Geotechnical Journal*, 37, 1000–1024.

19] HGI Hydro geophysics. "Dam monitoring Services." Damassessment.com

20] Guireli Netto, L., Gandolfo, O.C.B., Malagutti Filho, W., & Dourado, J.C. (2020). "Non-destructive investigation on small earth dams using geophysical methods: multichannel analysis of surface waves (MASW) and S-wave seismic refraction Tomography." *Brazilian Journal of Geophysics*, 38(1), 5-19. DOI: 10.22564/rbgf.v38i1.2031

21]

22]

23] Sunny, A.A., & Chris, O.A. (2019). "Insight into seismic refraction and electrical resistivity tomography techniques in subsurface investigation." *The Mining Geology Petroleum Engineering*. DOI: 10.17794/rgn.2019.1.9

24] Hauck, C. (2001). "Geophysical methods for detecting permafrost in high mountains." *Technical Note 171*. Zurich.

25] Pavoni, M., Boaga, J., Wagner, F.M., Bast, A., & Philips, M. (2023). "Characterization of rock glaciers environments combining structurally coupled and petrophysically-coupled joint inversions of electrical resistivity and seismic refraction dataset." *Journal of Applied Geophysics*. DOI: 10.1016/j.jappgeo.2023.105097

26] Uecker, R.K., Flinchum, B.A., Holbrook, W.S., & Carr, B.J. (2023). "Mapping bedrock topography: A seismic refraction survey and landscape analysis in the Laramie Range, Wyoming." *Front. Water*, 5:1057725. DOI: 10.3389/frwa.2023.1057725

27] Rucker, C., Gunther, T., & Wagner, F.M. (2017). "pyGIMLi: An open-source library for modelling and inversion in geophysics." *Computers & Geosciences*, Volume 109, December 2017, Pages 106-123. DOI: 10.1016/j.cageo.2017.07.011

28]

29] Xia, J. (2014). "Estimation of near-surface shear-wave velocities and quality factors using multichannel analysis of surface-wave methods." *Journal of Applied Geophysics*, Volume 103, Pages 140-151. DOI: 10.1016/j.jappgeo.2014.01.016

30]] https://prokon.com/kb/elastic-properties-of-soils/

31]

32] E. Cardarelli, M. Cercato, G. De Donno (2014). “Characterization of an earth-filled dam through the combined use of electrical resistivity tomography, P- and SH-wave seismic tomography and surface wave data”. Journal of Applied Geophysics 106 (2014) 87–95

33] Martina Germmato, Foti Sebastiano, Consentini Renato Maria (2021) Tesi di Laurea Magistrale. “Comportamento dinamico delle piccole dighe in terra del Piemonte: studio parametrico. Politecnico di Torino”

34] Montarosa SPA (2019) Certificato Collaudo “Lavori di construzione bacino per innevamento artificale “Alpe Forca” sul torrente fourcare in Loc. Franchey in Comuni di Ayas”

Appendix A

```
72 # shot/geophone points
#x              y
0.0000000e+00   0.0000000e+00
2.1037229e+00   0.0000000e+00
4.1983941e+00   0.0000000e+00
6.2509207e+00   0.0000000e+00
8.1744666e+00   0.0000000e+00
1.0064200e+01   0.0000000e+00
1.2149628e+01   0.0000000e+00
1.4042610e+01   0.0000000e+00
        .               .
        .               .
        .               .
1.2642437e+02   0.0000000e+00
1.2837716e+02   0.0000000e+00
1.2998583e+02   0.0000000e+00
1.3155484e+02   0.0000000e+00
1.3342304e+02   0.0000000e+00
901 # measurements
#s              g               t
1.0000000e+00   1.0000000e+00   1.0657819e-03
1.0000000e+00   2.0000000e+00   2.9774263e-03
1.0000000e+00   3.0000000e+00   5.2076782e-03
1.0000000e+00   4.0000000e+00   8.0751448e-03
1.0000000e+00   6.0000000e+00   1.2854256e-02
1.0000000e+00   7.0000000e+00   1.5403115e-02
        .               .               .
```

Figure 67 Illustrative example of ASCII file format containing source, geophone and picked first arrival travel time from Seismic Survey 1 to perform Seismic Inversion for SRT.

Appendix B

Nº	Disperse curve frequency	Vr	Uncertanty
1	15.6250000000000	1026	50
1	16.6015625000000	904	50
1	17.5781250000000	728	50
1	18.5546875000000	610	50
.	.	.	.
.	.	.	.
52	22.4609375000000	382	50
52	23.4375000000000	396	50
53	18.5546875000000	568	50
53	19.5312500000000	538	50
53	20.5078125000000	480	50
53	21.4843750000000	414	50
53	22.4609375000000	388	50
53	23.4375000000000	402	50

Figure 68 Illustrative Example of Vr matrix for Initial Vs Model for Seismic Survey 1.

```
5                       5                       5
15.0587359200000        17.1387423000000        19.2018644800000
1                       1                       1
0                       0                       0
1800                    1800                    1800
1900                    1900                    1900
2000                    2000                    2000
2200                    2200                    2200
2400                    2400                    2400
2600                    2600                    2600
0.250000000000000       0.250000000000000       0.250000000000000
0.250000000000000       0.250000000000000       0.250000000000000
0.250000000000000       0.250000000000000       0.250000000000000
0.250000000000000       0.250000000000000       0.250000000000000
0.250000000000000       0.250000000000000       0.250000000000000
0.250000000000000       0.250000000000000       0.250000000000000
0                       0                       0
5                       5                       5
5                       5                       5
5                       5                       5
5                       5                       5
5                       5                       5
300                     300                     300
500                     500                     500
700                     700                     700
900                     900                     900
1500                    1500                    1500
2000                    2000                    2000
```

Figure 69 Illustrative Example of Reference Model for Initial Vs Model from Survey Seismic 1 data.